VIP-producing enteric neurons interact with innate lymphoid cells to regulate feeding-dependent intestinal epithelial barrier functions

Jhimmy Talbot[1], Paul Hahn[1], Lina Kroehling[1], Henry Nguyen[1], Dayi Li[1], & Dan R. Littman[1,2]

[1]Molecular Pathogenesis Program, The Kimmel Center for Biology and Medicine of the Skirball Institute, New York University School of Medicine, New York, NY 10016, USA

[2]Howard Hughes Medical Institute, New York, NY 10016, USA.

Correspondence: dan.littman@med.nyu.edu

ABSTRACT

The intestinal mucosa serves as both a conduit for uptake of food-derived nutrients and microbiome-derived metabolites and as a barrier that prevents tissue invasion by microbes and tempers inflammatory responses to the myriad contents of the lumen. How the intestine coordinates physiological and immune responses to food consumption to optimize nutrient uptake while maintaining barrier functions remains unclear. Here, we describe how a gut neuronal signal triggered by food intake is integrated with intestinal antimicrobial and metabolic responses controlled by type 3 innate lymphoid cells (ILC3)[1-3]. Food consumption rapidly activates a population of enteric neurons that express vasoactive intestinal peptide (VIP)[4]. Projections of VIP-producing neurons (VIPergic neurons) in the lamina propria are in close proximity to clusters of ILC3 that selectively express VIP receptor type 2 (VIPR2 or VPAC2). ILC3 production of IL-22, which is up-regulated by commensal microbes such as segmented filamentous bacteria (SFB)[5-7], is inhibited upon engagement of VIPR2. As a consequence, there is a reduction in epithelial cell-derived antimicrobial peptide, but enhanced expression of lipid-binding proteins and transporters[8]. During food consumption, activation of VIPergic neurons thus enhances growth of epithelial-associated SFB and increases lipid absorption. Our results reveal a feeding- and circadian-regulated dynamic intestinal neuro-immune circuit that promotes a trade-off between IL-22-mediated innate immune protection and efficiency of nutrient absorption. Modulation of this pathway may hence be effective for enhancing resistance to enteropathogen[2,3,9] and for treatment of metabolic diseases.

42

43 **MAIN TEXT**

44 Type 3 innate lymphoid cells (ILC3) promote maintenance of intestinal immune and
45 metabolic homeostasis by integrating cytokine-mediated and glia-derived cues and,
46 through the production of IL-22 and other cytokines, conveying information from the
47 luminal microbiota to intestinal epithelial cells (IECs) and cells in the lamina propria [1-
48 3,5,10]. The activation of ILC3 is regulated by cytokines, including IL-23, IL-1β, and TL1A,
49 which are produced by mononuclear phagocytes and induced by intestinal microbe-
50 derived stimuli[5,7,11]. Cytokines produced by activated ILC3, particularly IL-22, support
51 the production of antimicrobial peptides (*e.g*. *RegIIIγ*) and mucin by IECs, ensuring
52 spatial segregation of microbes from the intestinal tissue[12,13]. This microbiota-ILC3-IEC
53 circuit promotes intestinal barrier function by controlling intestinal commensal microbiota
54 and mediating rapid protective responses to enteropathogens[2,3,9,12]. Different subtypes
55 of ILC3s are present within the intestinal lamina propria and are dispersed or in tertiary
56 lymphoid tissue clusters known as cryptopatches (CPs) and isolated lymphoid follicles
57 (ILFs)[14,15] . In perusing transcriptomic datasets of small intestinal ILCs, we noticed in
58 CCR6^{+} ILC3, which comprise the lymphoid tissue inducer (LTi) cells enriched in CPs
59 and ILFs, selective expression of multiple neurotransmitter/neuropeptide receptors and
60 genes related to axonal guidance and neuron differentiation when compared to CCR6^{neg}
61 ILC3 and NCR^{+} ILC3 (Fig. 1a and Extended Data Fig. 1a-c)[16,17]. This prompted us to
62 evaluate whether CCR6^{+} ILC3 in the intestinal lamina propria were associated with
63 neuronal projections from the enteric nervous system (ENS). The ENS is part of the
64 peripheral autonomic nervous system, which controls gastrointestinal functions by

65 promoting rapid gut responses to changes in the luminal compartment (e.g. food intake,
66 microbes, metabolites, etc.[18-22]). We observed that ILC3 in CPs/ILFs were in close
67 proximity to neuronal projections in the lamina propria (Fig. 1b-d and Supplementary
68 Videos 1,2). The CP/ILF-associated neuronal projections were positive for vasoactive
69 intestinal peptide upon staining with specific antibody (VIP, Fig. 1e and Extended Data
70 Fig. 2). We also observed association of VIPergic neurons and colonic lymphoid
71 patches (Extended Data Fig. 2 a,b). Indeed, ILC3 in CPs/ILFs were closer to VIPergic
72 neurons than to neurons positive for substance P or tyrosine hydroxylase (adrenergic)
73 (Fig. 1f and Extended Data Fig. 3). These anatomical findings, together with the
74 observation that CCR6^{+} ILC3, but not intestinal Th17 or γδT17 cells, express a high
75 amount of VIP receptor type 2 (*Vipr2*) (Fig. 1a and extended Data Figure 4a), prompted
76 us to investigate whether signaling from VIPergic neurons could modulate CCR6^{+} ILC3
77 functions and intestinal immune homeostasis.
78 We isolated ILC3 from the lamina propria of the small intestine of C57BL/6 mice
79 (Extended Data Fig. 4b) and observed that *in vitro* activation of VIPR2 inhibited IL-23-
80 induced production of IL-22 and IL-17A by CCR6^{+} ILC3 (Fig. 2a,b and Extended Data
81 Fig. 4c-e), although there was no effect on cell activation (marked by Sca-1 up-
82 regulation[5]) or on IL-22 production by CCR6^{neg} ILC3 (Extended Data Fig. 4f-h). In order
83 to investigate the *in vivo* role of VIPR2 activation on IL-22 production in unstimulated
84 (4h/37C) CCR6^{+} ILC3 functions, we generated mixed bone marrow chimeric mice
85 reconstituted with a 1:1 ratio of isotype-marked *Vipr2*$^{+/+}$ and *Vipr2*$^{-/-}$ cells. IL-22
86 production (assessed following inhibition of Golgi trafficking in unstimulated *ex vivo*
87 cultured cells) was observed in a greater proportion of *Vipr2*$^{-/-}$ CCR6^{+} ILC3 when

88 compared to *Vipr2*$^{+/+}$ CCR6^{+} ILC3 (Extended Data Fig 5a,b). We evaluated the
89 transcriptional profile of *Vipr2*$^{+/+}$ and *Vipr2*$^{-/-}$ CCR6^{+} ILC3 from these mice and
90 observed a marked difference between them, with up-regulation of genes involved in
91 retinoic acid-mediated signaling (*Rxra*) and translation initiation (*Eif5a*) in the absence of
92 *Vipr2* (Extended Data Fig 5c,d,e). We also generated mice with conditional deletion of
93 the gene encoding VIPR2 in ILC3 (*RORc(t)*^{Cre}*Vipr2*$^{fl/fl}$) and found that a larger proportion
94 and number of unstimulated CCR6^{+} ILC3 isolated from the ileum of these mice
95 produced IL-22 than cells isolated from WT (*RORc(t)*^{Cre}*Vipr2*$^{+/+}$) littermates (Fig. 2c and
96 Extended Data Fig. 5f-i). There was also a higher frequency of cells positive for IL-17A
97 in CCR6^{+} ILC3 from *RORc(t)*^{Cre}*Vipr2*$^{fl/fl}$ mice, although the amount was low compared to
98 IL-22 (Extended Data Fig. 5j,k). No differences were observed in the frequency of IL-
99 17A or IL-22 production among CD3^{+}RORγt^{+} cells (γδT17 and Th17 cells) (Extended
100 Data Fig. 5l,m). *RegIIIγ* mRNA, regulated by IL-22, was considerably higher in ileal
101 extracts enriched for intestinal epithelial cells (IECs) from *RORc(t)*^{Cre}*Vipr2*$^{fl/fl}$ mice when
102 compared to *RORc(t)*^{Cre}*Vipr2*$^{+/+}$ mice (Fig. 2d), suggesting that VIPergic signaling
103 through VIPR2 inhibits IL-22-mediated innate immune responses and epithelial cell
104 reactivity. In addition, small intestine villi and crypt lengths, as well as frequency of
105 proliferating cells (Ki67^{+}) in the crypts, were increased in *RORc(t)*^{Cre}*Vipr2*$^{fl/fl}$ mice
106 (Extended Data Fig. 5n-q), consistent with observations of the *in vivo* effects of chronic
107 IL-22 overexpression or treatment[23,24].
108 To determine whether direct modulation of VIPergic neurons (inhibition or activation)
109 could affect ILC3 function, we adopted a chemogenetic strategy utilizing mice
110 engineered to express designer receptors exclusively activated by designer drugs

111 (DREADD)[25] in VIP$^+$ cells (Extended Data Figure 6a-c). We expressed inhibitory
112 DREADD (hM4Di) in VIPergic neurons (*Vip*$^{IRES\text{-}Cre}$*hM4Di*$^{fl\text{-}stop\text{-}fl/+}$ mice) and observed a
113 higher frequency of IL-22-producing CCR6$^+$ILC3 in the small and large intestine at 24h
114 following VIPergic inhibition with the DREADD ligand clozapine-N-oxide (CNO, Fig. 2e,f
115 and Extended Data Figure 6d,e). In parallel, there was increased *RegIIIγ* mRNA
116 expression in ileal extracts enriched for IECs after inhibition of VIPergic neurons (Fig.
117 2g). Conversely, mice expressing the activating DREADD (hM3Dq) in VIPergic neurons
118 (*Vip*$^{IRES\text{-}Cre}$*hM3Dq*$^{fl\text{-}stop\text{-}fl/+}$ mice) had fewer IL-22$^+$ cells among the CCR6$^+$ ILC3 in the
119 small and large intestine, and lower *RegIIIγ* mRNA in IEC-enriched ileal extracts
120 following activation of VIPergic neurons (Fig. 2h-j and Extended Data Figure 6f).
121 However, differences were not observed in the frequency of IL-17A or IL-22 production
122 among CD3$^+$RORγt$^+$ cells (γδT17 and Th17) after activation of VIPergic neurons
123 (Extended Data Fig. 6g-h). Combined, these results indicate that VIPergic neurons
124 modulate intestinal immune homeostasis, acting through VIPR2 on CCR6$^+$ ILC3 to
125 inhibit cell activation and IL-22 production.
126 We next investigated whether alteration of VIPergic neuronal activity contributes to
127 changes of intestinal barrier function during intestinal colonization with an
128 enteropathogen. As previously described[26], following infection with *Citrobacter*
129 *rodentium* there was increased *Vip* mRNA expression in the proximal colon and cecum
130 and of VIP amounts in the portal vein, but not in the peripheral blood (Extended Data
131 Fig. 7a-c), suggesting an increase in VIPergic activity in the intestinal tissue. Oral
132 gavage of mice with a relatively low dose of *C. rodentium* ($2x10^9$ CFU) is tolerated by
133 mice with an intact immune system. However, DREADD-mediated activation of VIPergic

134 neurons during the first 4 days of infection led to increased bacterial translocation to the
135 spleen and liver (Fig. 2k,l) and resulted in reduced survival (Fig. 2m and Extended Data
136 Fig 7d), despite only a moderate increase in the amount of luminal *C. rodentium*
137 (Extended Data Fig. 7e). Gavage with a high dose of *C. rodentium* ($4x10^{10}$ CFU)
138 resulted in large amounts of bacteria that translocated to the liver and spleen (9d.p.i.)
139 (Fig. 2n,o). DREADD-mediated inhibition of VIPergic neurons provided substantial
140 protection from bacterial breach of the intestinal barrier without affecting the bacterial
141 burden in the feces (Fig 2n,o and Extended Data Fig. 7f). Moreover, treatment with
142 recombinant murine IL-22 reversed the effect of DREADD-mediated activation of
143 VIPergic neurons on mortality and bacterial translocation (Extended Data Fig. 7g,h). In
144 addition, *RORc(t)*^{Cre}*Vipr2*$^{fl/fl}$ mice exhibited enhanced protection from bacterial breach of
145 the intestinal barrier after gavage with a high dose of *C. rodentium* ($4x10^{10}$ CFU) when
146 compared with *RORc(t)*^{Cre}*Vipr2*$^{+/+l}$ mice (Extended Data Figure 7i,j). Activation of
147 VIPergic neurons during the events that follow infection with enteropathogens may
148 therefore be an important contributor to intestinal barrier breakdown, which could be
149 mitigated by inhibition of VIPergic signaling in ILC3.
150 These results suggested the existence of physiological signals that promote
151 activation of VIPergic neurons during homeostasis, with consequent tonic inhibition of
152 $CCR6^+$ ILC3. Food ingestion has been reported to rapidly signal VIP release in the
153 intestine[4]. Indeed, we observed a greater amount of VIP in the ileum of mice sampled
154 during the vivarium's dark-phase as compared to the light-phase, which correspond to
155 periods of food consumption and resting, respectively (Extended Data Fig. 8a). Due to
156 the *ad libitum* feeding scheme, approximately 15% of daily food intake occurs during the

157 light-phase/resting period[27]. To dissect the effect of food intake on the VIPergic immune
158 inhibitory axis and to reduce the noise created by feeding during the resting period, we
159 restricted food availability for two weeks to alternating 12h cycles of feeding and fasting.
160 To dissociate the effects of light/dark cycles from time of feeding, food was available to
161 a group of mice only during the dark-phase (night-fed mice, ZT12-ZT0/6PM-6AM), while
162 another group had food available only during the light-phase (day-fed mice, ZT0-
163 ZT12/6AM-6PM). Using this scheme, we observed more VIP in the portal vein, but not
164 in the peripheral blood, after 6h of food availability when compared to mice fasted for
165 6h, regardless of whether mice were fed during the light phase (ZT 6) or during the dark
166 phase (ZT 18) (Extended Data Fig. 8b,c). In turn, the frequency of IL-22^{+} CCR6^{+} ILC3
167 was reduced during the periods of food consumption (at 6h of feeding) relative to fasting
168 periods (fasted for 6h), independently of light-dark cycles (Fig. 3a,b).
169 Using the same feeding scheme, we observed among CCR6^{+} ILC3 from
170 *RORc(t)*^{Cre}*Vipr2*$^{+/+}$ mice a reduced frequency of IL-22^{+} cells at 6h after start of food
171 consumption (ZT 18) when compared to mice fasted for 6h (ZT 6) (Fig 3c,d). In contrast,
172 there was no difference in frequency of IL-22^{+} cells in the CCR6^{+} ILC3 from
173 *RORc(t)*^{Cre}*Vipr2*$^{fl/fl}$ littermates with or without feeding. The same results were observed
174 with mixed bone marrow chimeric mice (Extended Data Figure 8d,e). This is consistent
175 with VIPR2 signaling-dependent inhibition of IL-22 production in CCR6^{+} ILC3 following
176 food intake. This conclusion was further supported by the observed reduction in the
177 frequency of IL-22^{+} CCR6^{+} ILC3 at 6h following intragastric delivery of a liquid test diet,
178 but not control saline, during the light-phase period (ZT1-ZT7) (Fig 3e,f). Furthermore,
179 DREADD-mediated inhibition of VIPergic neurons abrogated the effect of the test diet

180 on ILC3 (Fig. 3e and 3f). These results suggest a fast and dynamic temporal control of
181 intestinal CCR6^{+} ILC3 function promoted by food intake-mediated activation of VIPergic
182 signaling and VIPR2.

183 Because IL-22 acts on intestinal epithelial cells to regulate barrier functions,
184 including their interactions with commensal microbiota, we next examined whether the
185 neuroimmune inhibitory circuit promoted by food consumption influences host-microbial
186 interactions. There was an IL-22-dependent elevation of *RegIIIγ* mRNA expression in
187 IEC-enriched ileal extracts from mice fasted for 12h as compared to those fed during
188 that time frame (Fig. 4a). In parallel, food consumption had a striking effect on the
189 morphology of the ileal epithelium-associated segmented filamentous bacteria (SFB)
190 (Fig. 4b-c and Extended Data Fig. 9a-c). SFB attached to IECs had long segmented
191 filaments after 12h of food consumption, independently of light/dark cycles. However, in
192 the ileum of mice fasted for 12h, independently of light-cycle, epithelium-associated
193 SFB had few segments and were stubble-like. A strong effect of feeding/fasting cycles
194 was also observed in the composition of the fecal microbiota, independently of light-
195 cycle (Extended Data Fig. 9d,e). Indeed, there was an increase in the
196 *Firmicutes/Bacteroidetes* ratio in the feces of mice after 12h of feeding compared to 12h
197 of fasting.

198 Short-term blockade with α-IL-22 not only reduced *RegIIIγ* mRNA expression in the
199 ileal extracts enriched for IECs of mice during fasting, but also prevented control of SFB
200 growth upon food restriction (Fig. 4d). In *RORc(t)*^{Cre}*Vipr2*$^{fl/fl}$ mice, which have increased
201 IL-22 production, SFB failed to form segmented filaments even after 12h of food
202 consumption (Fig. 4e,f and Extended Data Figure 10a). Moreover, we observed a

203 reduced *Firmicutes/Bacteroidetes* ratio in the ileal fecal matter of *RORc(t)*^{Cre}*Vipr2*$^{fl/fl}$
204 mice after 12h feeding compared to *RORc(t)*^{Cre}*Vipr2*$^{+/+}$ mice (Extended Data Figure
205 10b-e). These results suggest that VIPergic signaling regulate commensal microbiota by
206 modulating cryptopatch-associated ILC3 in response to food consumption.

207 As IL-22 was recently shown to regulate lipid metabolism[8], at least in part by
208 controlling genes involved in lipid transport, we examined the role of the VIPergic-ILC3-
209 IL-22 circuit in lipid absorption. Mice were adapted for 2 weeks to 12h restricted feeding
210 during light or dark cycles and were then gavaged with ^{3}H-triolein following feeding or
211 fasting. Mice that had been fed for 12h absorbed more of the triglyceride than mice
212 fasted for 12h, although there was some effect of circadian regulation (light/dark
213 adaptation) (Extended Data Fig. 11a,b). Expression of mRNAs for proteins associated
214 with fatty-acid/lipid uptake and transport (e.g. *Fabp2*) was lower in IEC-enriched ileal
215 extracts from mice that were food-restricted for 12h compared to fed mice (Fig. 4g), in
216 inverse relationship to *RegIII*γ mRNA (Fig 4a). Moreover, short-term treatment with α-IL-
217 22 during the fasting period increased ^{3}H-triolein absorption and the expression of lipid
218 transporters in ileal extracts enriched for IECs (Fig 4g,h).

219 The effect of food intake on IEC-dependent lipid absorption was dependent on
220 VIPergic signaling of ILC3, since expression of *Fabp2* and *Cd36* mRNAs, ^{3}H-triolein
221 absorption, and concentrations of circulating plasma triglycerides were substantially
222 reduced in *RORc(t)*^{Cre}*Vipr2*$^{fl/fl}$ mice when compared to *RORc(t)*^{Cre}*Vipr2*$^{+/+}$ littermates
223 after 12h of feeding (ZT 0) (Figures 4i-k). Moreover, *RORc(t)*^{Cre}*Vipr2*$^{fl/fl}$ mice had
224 reduced weight compared to their *RORc(t)*^{Cre}*Vipr2*$^{+/+}$ littermates (Extended Data 11c,d),
225 similarly to transgenic mice that constitutively express high levels of IL-22[28]. Finally,

226 continuous intragastric delivery of a liquid test diet for 6h during the light phase period
227 led to an increase in serum triglycerides, which was blocked by DREADD-mediated
228 inhibition of VIPergic neurons (Fig. 4l).

229 These results reveal an important neuro-immune circuit in which feeding-activated
230 VIPergic neurons antagonize microbiota-dependent CCR6^{+} ILC3 function, resulting in
231 reduced IL-22 production and increased efficiency of lipid absorption (Extended Data
232 Figure 11e,f). The benefit of greater nutrient acquisition comes at the expense of
233 reduced IL-22-promoted antimicrobial functions, illustrated by susceptibility to
234 enteropathic bacteria, rapid growth of epithelial-associated commensal SFB, and
235 broader changes in the luminal commensal composition (increased
236 *Firmicutes/Bacteroidetes* ratio). Whether the host derives benefit from the reduced anti-
237 microbial activity is unclear, although it may enable bacteria-dependent generation of
238 essential metabolites[29] and vitamins that would be readily absorbed. It will be of interest
239 to determine in the future the global metabolic consequences following chronic
240 activation of ILC3/IL-22 in the absence of VIPR2 signaling. Since enteric glial cells
241 (EGCs) are reported to secrete factors that act as activators of ILC3 functions[10], it will
242 additionally be important to determine whether VIPergic neurons and EGCs coordinate
243 antagonistic signals to promote efficient modulation of ILC3-mediated intestinal barrier
244 functions, and also how neural development-associated factors expressed by ILC3 (e.g.
245 *Cntn1*, *Sema3d*, *Bmp2*) contribute to formation of neuro-immune cell units in
246 cryptopatches/ILFs.

247 The mechanism by which the presence of food in the intestinal lumen is sensed and
248 promotes VIPergic activation is still unclear, and microbial[30,31], nutritional[4] or mechanical

249 stimuli[32], acting peripherally or by way of the central nervous system, may be
250 responsible for this. The VIP system has been implicated in circadian regulation
251 centrally, as VIPR2 is required for expression of the core clock genes in the
252 suprachiasmatic nuclei of the hypothalamus, and in the periphery, with circadian
253 oscillation of IL-5 and IL-13 production by ILC2 and feeding-associated eosinophil
254 recruitment in lung and gut mucosa[33,34]. While our study highlights the importance of
255 food intake in regulating VIPergic neurons, there is also a light-dependent contribution
256 to the efficiency of lipid absorption, as there was only a partial effect when the feeding
257 cycle was reversed. We therefore cannot rule out an additional role for central or
258 peripheral clock functions[35] independent of the enteric VIP-ILC3 circuit.
259 Our results suggest that disturbances in feeding schedules could reduce intestinal
260 barrier functions and promote dysbiosis and at the same time contribute to metabolic
261 inbalance by chronic activation of VIPergic neurons. Moreover, enteropathogens may
262 hijack this neuro-immune circuit and reduce intestinal barrier functions, facilitating
263 intestinal colonization. In these scenarios, VIPR2 inhibitors may be valuable therapeutic
264 tools to reduce lipid absorption or enforce the barrier during acute gastrointestinal
265 infections.
266

267 **Acknowledgements**

268 We thank members of the Littman lab and Juan J. Lafaille for valuable discussion. We
269 thank S.Y. Kim and the NYU Rodent Genetic Engineering Laboratory (RGEL) for
270 generating the mutant mice, Cindy Loomis and the Experimental Pathology Research
271 Laboratory of NYULMC for histology of small intestine samples, and Adriana Heguy and

272 the Genome Technology Center (GTC) for RNA sequencing. We also thank F-X. Liang,
273 J. Sall, C. Petzold and K. Dancel at the Microscopy Laboratory Core for timely
274 preparation of the scanning electron microscopy images, and M. Cammer and Y. Deng
275 for the help with optical microscopy. The Microscopy Core and the GTC are partially
276 supported by NYU Cancer Center Support Grant NIH/NCI P30CA016087 at the Laura
277 and Isaac Perlmutter Cancer Center, S10 RR023704-01A1 and NIH S10 ODO019974-
278 01A1. The Experimental Pathology Research Laboratory is supported by National
279 Institutes of Health Shared Instrumentation grants S10OD010584-01A1 and
280 S10OD018338-01. This study benefitted from data assembled by the ImmGen
281 Consortium. This work was supported by the Pew Latin American Fellows program
282 (J.T.), the Helen and Martin Kimmel Center for Biology and Medicine (D.R.L.); and
283 National Institutes of Health grant R01DK103358 (D.R.L.). D.R.L. is an Investigator of
284 the Howard Hughes Medical Institute.
285

286 **Author Contributions**

287 J.T. and D.R.L. designed the study and analyzed the data. J.T. performed the
288 experiments with assistance from P.H. and D.L., H.N. contributed to the feeding
289 experiments, and L.K. performed the bioinformatics analyses. J.T. and D.R.L. wrote the
290 manuscript. D.R.L. supervised the research.
291

292 **FIGURE LEGENDS**

293 **Figure 1. Processes of VIP-producing enteric neurons are in close proximity to *Vipr2*-**
294 **expressing ILC3 within cryptopatches. a,** Heatmap of differentially expressed neural-related

295 genes between intestinal CCR6^{+} ILC3 and CCR6^{neg} ILC3 (Fold change $\geq$ 2, *p-value <0.05,*
296 GSE116092). Color scale is based on normalized read counts. Genes are listed on the right
297 hand margin ranked based on the relative fold change, and color coded: Green:
298 Neurotransmitter/neuropeptide receptors, Blue: genes related to nervous system
299 development/axonal guidance and contact. Expression in other ILC subsets is included for
300 comparison. **b-d,** Representative confocal images from the small intestine of *RORc(t)*$^{EGFP/+}$
301 mice show clusters of intestinal ILC3 (cryptopatch) in close proximity to enteric neurons in the
302 small intestine lamina propria (see supplementary videos 1 and 2). Pan-neuronal marker: β3-
303 tubulin^{+} (red), ILC3: GFP^{+}TCRβ^{neg} (green and blue, respectively). n=4 mice, all the 110 ILC3
304 clusters analyzed exhibited β3-tubulin^{+} fibers interacting with ILC3. **e,** Neurochemical code of
305 cryptopatch-associated enteric neurons. Representative confocal images from the small
306 intestine of *RORc(t)*$^{EGFP/+}$ mice show cryptopatch-associated enteric neurons are positive for
307 VIP. Neurons: β3-tubulin^{+} (red), VIP^{+} (green); ILC3: GFP^{+} (blue). n=4 mice, 40 ILC3 clusters
308 analyzed, with all displaying VIP^{+} β3-tubulin^{+} fibers interacting with ILC3.
309
310 **Figure 2. VIPergic signaling promotes reduction of mucosal barrier function by**
311 **VIPR2-dependent inhibition of CCR6^{+} ILC3. a, b,** Representative FACS plot (**a**) and
312 summaries (**b**) indicating IL-22 expression in purified CCR6^{+} ILC3 after *in vitro* IL-23
313 stimulation with/without VIPR2 agonist ligands. BAY: BAY-559837, VIP: vasoactive
314 intestinal peptide. **P*<0.05 and ****P*<0.001 (*t-test*). Data are representative of three
315 independent experiments. **c,** Number of IL-22^{+} CCR6^{+} ILC3 present in the ileum of
316 *RORc(t)*^{Cre}*Vipr2*$^{+/+}$ and *RORc(t)*^{Cre} *Vipr2*$^{fl/f}$ mice. *RORc(t)*^{Cre}*Vipr2*$^{+/+}$: 8; *RORc(t)*^{Cre}
317 *Vipr2*$^{fl/f}$: 6. Data are representative of 2 independent experiments, ***P*<0.01 (*t-test*). **d,**

318 Normalized *RegIIIγ* mRNA expression in IEC-enriched ileal extracts from
319 *RORc(t)*^{Cre}*Vipr2*$^{+/+}$ and *RORc(t)*^{Cre} *Vipr2*$^{fl/f}$ mice. *RORc(t)*^{Cre}*Vipr2*$^{+/+}$: 5; *RORc(t)*^{Cre}
320 *Vipr2*$^{fl/f}$: 5. Data are representative of 3 independent experiments,***P<0.001 (*t-test*). **e-**
321 **g,** Effect of VIPergic inhibition on ILC3 and IECs. Representative FACS plot (**e**) and
322 summary (**f**) indicating IL-22 expression in CCR6^{+} ILC3 from the ileum of *Vip*$^{IRES-Cre}$
323 *hM4Di*$^{fl-stop-fl/+}$ mice (DREADD for VIPergic inhibition) at 24h following treatment with
324 vehicle or CNO (Clozapine-N-oxide, DREADD ligand). Vehicle: n=5, CNO: n=5.
325 **P<0.01 (*t-test*). Data representative of three independent experiments. **g,** Normalized
326 *RegIIIγ* mRNA expression in ileal extracts enriched for IECs at 24h following treatment.
327 Vehicle: n=3, CNO: n=3. *P<0.05 (*t-test*). Data representative of two independent
328 experiments. **h-j,** Effect of VIPergic activation on ILC3 and ileal extracts enriched for
329 IECs. Representative FACS plot (**h**) and summaries (**i**) indicating IL-22 expression in
330 CCR6^{+} ILC3 from ileum of *Vip*$^{IRES-Cre}$ *hM3Dq*$^{fl-stop-fl/+}$ (DREADD for VIPergic activation) at
331 24h following the treatment with vehicle or CNO. Vehicle: 6, CNO: 7. **P<0.01 (*t-test*). **j,**
332 Normalized *RegIIIγ* mRNA expression in ileal extracts enriched for IECs at 24h following
333 treatment with vehicle or CNO. Vehicle: 7, CNO: 6. *P<0.05 (*t-test*). Data representative
334 of three independent experiments. **k, l,** Dissemination of *C. rodentium* to the (**k**) spleen
335 and (**l**) liver in *Vip*$^{IRES-Cre}$ *hM3Dq*$^{fl-stop-fl/+}$ mice treated with vehicle or CNO (1mg/Kg, daily)
336 for 4 days post-intragastric infection with $2x10^{9}$ CFU. Log_{10} Colony Forming Units (CFU)
337 of *C. rodentium* 9 days post-oral innoculation (9 d.p.i.). Dotted line: limit of detection.
338 ***P=0.0009 and ****P<0.0001, (*Mann-Whitney test*). Vehicle: n=11 (Positive for *C.*
339 *rodentium:* spleen: 6/11, liver: 8/11), CNO: n=9 (Positive for *C. rodentium:* spleen and

340 liver: 9/9). Data representative of two independent experiments. **m,** Survival rates for *C.*
341 *rodentium*-infected *Vip*$^{IRES\text{-}Cre}$ *hM3Dq*$^{fl\text{-}stop\text{-}fl/+}$ mice treated with vehicle or CNO (1mg/Kg,
342 daily, 1-4 d.p.i.: blue rectangle). Vehicle: n=11, CNO: n=11. Data representative of three
343 independent experiments. ****P<0.0001 *(Mantel-Cox test*). **n, o,** Bacterial dissemination
344 to the (**n**) spleen and (**o**) liver of *Vip*$^{IRES\text{-}Cre}$ *hM4Di*$^{fl\text{-}stop\text{-}fl/+}$ mice treated with vehicle or
345 CNO (1mg/Kg, daily, 1-4 days post-intragastric infection with $4x10^{10}$ CFU of *C.*
346 *rodentium*). Log_{10} CFU at 9 d.p.i. Dotted line: limit of detection. Vehicle: n=8 (Positive for
347 *C. rodentium:* spleen: 8/8, liver: 8/8), CNO: n=7 (Positive for *C. rodentium:* spleen: 1/7,
348 liver: 1/7). ***P=0.0006 (spleen) and ***P=0.0005 (liver) (*Mann-Whitney test*). Data
349 representative of two independent experiments. **k,l,n,o**: For visualization in the
350 logarithm scale, CFU counts of 0 were attributed a value of 1.
351
352
353 **Figure 3. Feeding reduces IL-22 production by CCR6^{+}ILC3 through activation of**
354 **VIPergic neurons. a, b,** Representative FACS plot (**a**) and summaries (**b**) indicating IL-22
355 expression among CCR6^{+} ILC3 from the ileum of mice at 6h after feeding or fasting, at ZT6
356 and ZT18. N=5, *P<0.05 (*t-test*). Data are representative of two independent experiments. **c,**
357 **d,** Representative FACS plot (**c**) and summaries (**d**) indicating IL-22 expression by CCR6^{+}
358 ILC3 from *RORc(t)*^{Cre}*Vipr2*$^{+/+}$ or *RORc(t)*^{Cre}*Vipr2*$^{fl/fl}$ mice at 6h after fasting or 6h after feeding
359 (ZT 18). **P<0.01 (*paired t-test*). Data shown are pooled from two independent experiments
360 and representative of three independent experiments. **e, f,** Representative FACS plot (**e**) and
361 summaries (**f**) indicating IL-22 expression in CCR6^{+} ILC3 from the ileum of *Vip*$^{IRES\text{-}Cre}$ *hM4Di*$^{fl\text{-}}$

362 $^{stop\text{-}fl/+}$ mice (DREADD for VIPergic inhibition). Mice were treated with vehicle or CNO (1mg/Kg)
363 and 30 minutes later were fed by intragastric administration of saline (0.4 mL each 45 min, for
364 6 h) or Liquid Test Diet (500 mg/mL, 0.4mL each 45 minutes, for 6 h). N=4, ***P*<0.01 (*t-test*).
365 Data shown are representative of three independent experiments.
366
367 **Figure 4. Dynamic regulation of commensal bacterial growth and lipid**
368 **absorption by feeding-dependent modulation of the VIP-VIPR2-IL-22 axis. a,**
369 Normalized *RegIIIγ* mRNA expression in IECs from mice treated with IgG or α-IL-22
370 (10mg/Kg) during the feeding period (Fed for 12h: Treated from ZT 12->ZT 0) or during
371 the fasting period (Fasted for 12h: Treated from ZT 0->ZT 12). Data pooled from 2
372 independent experiments: Fed IgG1: N=8, Fed α-IL-22: N=8, Fasted IgG1: N=8, Fasted
373 α-IL-22: N=7, **P*<0.05 and ***P*<0.01 (*t-test*). **b, c,** Representative scanning electron
374 microscopy (SEM) images (**b**) of epithelium-associated commensal SFB in the ileum of
375 mice 12h after fasting or feeding at the end of the dark-phase (ZT 0) and the light-phase
376 (ZT 12) and (**c**) measurements of SFB filament lengths. N=3, data representative of 2
377 independent experiments,****P*<0.001 (*t-test*). **d,** SFB length in the ileum of mice treated
378 with IgG or α-IL-22 (10mg/Kg) during the feeding period (Fed for 12h: ZT 12->ZT 0) or
379 during the fasting period (Fast for 12h: ZT 0->ZT 12). N= 3, data representative of 2
380 independent experiments,****P*<0.001 (*t-test*). **e,f,** Representative **(e)** SEM images of
381 epithelium-associated SFB in the ileum of *RORc(t)*^{Cre} *Vipr2*$^{+/+}$ and *RORc(t)*^{Cre} *Vipr2*$^{fl/fl}$
382 mice fed for 12h and **(f)** measurement of bacterial filament lengths. N= 3, ****P*<0.001
383 (*t-test*). **g,** Normalized *Fabp2* mRNA expression in IEC-enriched ileal extracts from mice
384 treated with IgG or α-IL-22 (10mg/Kg) during the fasting period (Fasted for 12h: Treated

385 from ZT 0->ZT 12). Data representative of 3 independent experiments: Fed IgG1: N=8,
386 Fed α-IL-22: N=8, Fast IgG1: N=8, Fed α-IL-22: N=7. *P<0.05 and ****P<0.0001 (t-
387 student). **h,** Plasma ^{3}H CPM (counts per minute) in 12h fasted mice after gavage
388 with ^{3}H-triolein (2uCi/mice in 200ul of 20% Intralipid). Mice were treated with IgG or α-
389 IL-22 (10mg/Kg) during the fasting period (Fasted for 12h: Treated from ZT 0->ZT 12).
390 Data representative of 2 independent experiments. N=4, ***P<0.001 (*two-way ANOVA*).
391 **i, j,** Normalized *Fabp2* and *Cd36* mRNA expression in IEC-enriched ileal extracts from
392 (**i**) and plasma triglyceride content (**j**) in 12h fed *RORc(t)*^{Cre} *Vipr2*$^{+/+}$ (N=5) and
393 *RORc(t)*^{Cre} *Vipr2*$^{fl/fl}$ (N=4) mice**.** **P<0.05 and **P<0.01 (*t-test*). **k,** Plasma ^{3}H CPM in 12h
394 fed *RORc(t)*^{Cre} *Vipr2*$^{+/+}$ (N=3) and *RORc(t)*^{Cre} *Vipr2*$^{fl/fl}$ (N=3) mice after gavage with ^{3}H-
395 triolein. Data representative of 2 independent experiments,***P<0.001, (*two-way*
396 *ANOVA*). **l,** Plasma triglyceride content in *Vip*$^{IRES\text{-}Cre}$ *hM4Di*$^{fl\text{-}stop\text{-}fl/+}$ mice (DREADD for
397 VIPergic inhibition) after gavage with Saline (0.4 mL/each 45 minutes, for 6 hours) or
398 Liquid Test Diet (500 mg/mL, 0.4mL/each 45 minutes, for 6 hours). Vehicle: N=5, CNO:
399 N=4. Data representative of 2 independent experiments, **P<0.01, (*t-test*).
400
401

402 **REFERENCES**

403 1. Constantinides MG. Interactions between the microbiota and innate and innate-like
404 lymphocytes. *J Leukoc Biol.* 2018;103(3):409-419.
405 2. Sonnenberg GF. Regulation of intestinal health and disease by innate lymphoid cells. *Int*
406 *Immunol.* 2014;26(9):501-507.
407 3. Spits H, Cupedo T. Innate lymphoid cells: emerging insights in development, lineage
408 relationships, and function. *Annu Rev Immunol.* 2012;30:647-675.
409 4. Chayvialle JA, Miyata M, Rayford PL, Thompson JC. Effects of test meal, intragastric
410 nutrients, and intraduodenal bile on plasma concentrations of immunoreactive
411 somatostatin and vasoactive intestinal peptide in dogs. *Gastroenterology.* 1980;79(5 Pt
412 1):844-852.
413 5. Sano T, Huang W, Hall JA, et al. An IL-23R/IL-22 Circuit Regulates Epithelial Serum
414 Amyloid A to Promote Local Effector Th17 Responses. *Cell.* 2015;163(2):381-393.
415 6. Savage AK, Liang HE, Locksley RM. The Development of Steady-State Activation Hubs
416 between Adult LTi ILC3s and Primed Macrophages in Small Intestine. *J Immunol.*
417 2017;199(5):1912-1922.
418 7. Longman RS, Diehl GE, Victorio DA, et al. CX(3)CR1(+) mononuclear phagocytes support
419 colitis-associated innate lymphoid cell production of IL-22. *J Exp Med.* 2014;211(8):1571-
420 1583.
421 8. Mao K, Baptista AP, Tamoutounour S, et al. Innate and adaptive lymphocytes
422 sequentially shape the gut microbiota and lipid metabolism. *Nature.*
423 2018;554(7691):255-259.
424 9. Zheng Y, Valdez PA, Danilenko DM, et al. Interleukin-22 mediates early host defense
425 against attaching and effacing bacterial pathogens. *Nat Med.* 2008;14(3):282-289.
426 10. Ibiza S, Garcia-Cassani B, Ribeiro H, et al. Glial-cell-derived neuroregulators control type
427 3 innate lymphoid cells and gut defence. *Nature.* 2016;535(7612):440-443.
428 11. Mortha A, Chudnovskiy A, Hashimoto D, et al. Microbiota-dependent crosstalk between
429 macrophages and ILC3 promotes intestinal homeostasis. *Science.*
430 2014;343(6178):1249288.
431 12. Hooper LV, Littman DR, Macpherson AJ. Interactions between the microbiota and the
432 immune system. *Science.* 2012;336(6086):1268-1273.
433 13. Dudakov JA, Hanash AM, van den Brink MR. Interleukin-22: immunobiology and
434 pathology. *Annu Rev Immunol.* 2015;33:747-785.
435 14. Eberl G, Marmon S, Sunshine MJ, Rennert PD, Choi Y, Littman DR. An essential function
436 for the nuclear receptor RORgamma(t) in the generation of fetal lymphoid tissue inducer
437 cells. *Nat Immunol.* 2004;5(1):64-73.
438 15. Gury-BenAri M, Thaiss CA, Serafini N, et al. The Spectrum and Regulatory Landscape of
439 Intestinal Innate Lymphoid Cells Are Shaped by the Microbiome. *Cell.* 2016;166(5):1231-
440 1246 e1213.
441 16. Pokrovskii M, Hall JA, Ochayon DE, et al. Characterization of Transcriptional Regulatory
442 Networks that Promote and Restrict Identities and Functions of Intestinal Innate
443 Lymphoid Cells. *Immunity.* 2019.

444 17. Heng TS, Painter MW, Immunological Genome Project C. The Immunological Genome
445 Project: networks of gene expression in immune cells. *Nat Immunol.* 2008;9(10):1091-
446 1094.
447 18. Furness JB. The enteric nervous system and neurogastroenterology. *Nat Rev*
448 *Gastroenterol Hepatol.* 2012;9(5):286-294.
449 19. Muller PA, Koscso B, Rajani GM, et al. Crosstalk between muscularis macrophages and
450 enteric neurons regulates gastrointestinal motility. *Cell.* 2014;158(2):300-313.
451 20. Cardoso V, Chesne J, Ribeiro H, et al. Neuronal regulation of type 2 innate lymphoid cells
452 via neuromedin U. *Nature.* 2017;549(7671):277-281.
453 21. Klose CSN, Mahlakoiv T, Moeller JB, et al. The neuropeptide neuromedin U stimulates
454 innate lymphoid cells and type 2 inflammation. *Nature.* 2017;549(7671):282-286.
455 22. Margolis KG, Gershon MD. Enteric Neuronal Regulation of Intestinal Inflammation.
456 *Trends Neurosci.* 2016;39(9):614-624.
457 23. Zwarycz B, Gracz AD, Rivera KR, et al. IL22 Inhibits Epithelial Stem Cell Expansion in an
458 Ileal Organoid Model. *Cell Mol Gastroenterol Hepatol.* 2019;7(1):1-17.
459 24. Zha JM, Li HS, Lin Q, et al. Interleukin 22 Expands Transit-Amplifying Cells While
460 Depleting Lgr5(+) Stem Cells via Inhibition of Wnt and Notch Signaling. *Cell Mol*
461 *Gastroenterol Hepatol.* 2019;7(2):255-274.
462 25. Roth BL. DREADDs for Neuroscientists. *Neuron.* 2016;89(4):683-694.
463 26. Conlin VS, Wu X, Nguyen C, et al. Vasoactive intestinal peptide ameliorates intestinal
464 barrier disruption associated with Citrobacter rodentium-induced colitis. *Am J Physiol*
465 *Gastrointest Liver Physiol.* 2009;297(4):G735-750.
466 27. Kohsaka A, Laposky AD, Ramsey KM, et al. High-fat diet disrupts behavioral and
467 molecular circadian rhythms in mice. *Cell Metab.* 2007;6(5):414-421.
468 28. Park O, Wang H, Weng H, et al. In vivo consequences of liver-specific interleukin-22
469 expression in mice: Implications for human liver disease progression. *Hepatology.*
470 2011;54(1):252-261.
471 29. Smith PM, Howitt MR, Panikov N, et al. The microbial metabolites, short-chain fatty
472 acids, regulate colonic Treg cell homeostasis. *Science.* 2013;341(6145):569-573.
473 30. McVey Neufeld KA, Perez-Burgos A, Mao YK, Bienenstock J, Kunze WA. The gut
474 microbiome restores intrinsic and extrinsic nerve function in germ-free mice
475 accompanied by changes in calbindin. *Neurogastroenterol Motil.* 2015;27(5):627-636.
476 31. McVey Neufeld KA, Mao YK, Bienenstock J, Foster JA, Kunze WA. The microbiome is
477 essential for normal gut intrinsic primary afferent neuron excitability in the mouse.
478 *Neurogastroenterol Motil.* 2013;25(2):183-e188.
479 32. Chayvialle JA, Miyata M, Rayford PL, Thompson JC. Release of vasoactive intestinal
480 peptide by distention of the proximal stomach in dogs. *Gut.* 1980;21(9):745-749.
481 33. Harmar AJ, Marston HM, Shen S, et al. The VPAC(2) receptor is essential for circadian
482 function in the mouse suprachiasmatic nuclei. *Cell.* 2002;109(4):497-508.
483 34. Nussbaum JC, Van Dyken SJ, von Moltke J, et al. Type 2 innate lymphoid cells control
484 eosinophil homeostasis. *Nature.* 2013;502(7470):245-248.
485 35. Godinho-Silva C, Domingues RG, Rendas M, et al. Light-entrained and brain-tuned
486 circadian circuits regulate ILC3s and gut homeostasis. *Nature.* 2019;574(7777):254-258.
487

488 **METHODS**

489 *Mice*

490 C57Bl/6 mice were obtained from Taconic Farm. All transgenic mice were bred and
491 maintained in the animal facility of the Skirball Institute (New York University School of
492 Medicine) in specific pathogen-free conditions. *hM3Dq*$^{fl\text{-}stop\text{-}fl}$ mice (CAG-LSL-Gq-
493 DREADD, Jax #026220), *hM4Di*$^{fl\text{-}stop\text{-}fl}$ mice (CAG-LSL-Gi-DREADD, Jax #026219),
494 *VIP*$^{IRES\text{-}Cre}$ mice (B6J.Vip-IRES-Cre, Jax #031628), *tdTomato*$^{f/\text{-}stop\text{-}fl}$ (CAG-tdTomato,
495 JAX #007914) and CD45.1 mice (*B6.SJL-Ptprca Pepcb/BoyJ*, Jax# 002014) were
496 purchased from Jackson Laboratories. *RORc(t)*$^{EGFP/+}$ and *RORc(t)*^{Cre} mice were
497 generated in our laboratory and previously described[14,36]. BAC-transgenic *Rorc(t)-Gfp*^{TG}
498 were generated by G. Eberl's lab[37] and used for evaluation of *Vipr2* mRNA expression
499 in different populations of RORγt^{+} lymphoid cells purified by FACS sorting. *Vipr2*$^{-/-}$ mice
500 (Jax# 031332) were purchased from Jackson Laboratories and were maintained in a
501 CD45.2 background or were bred with CD45.1 (*B6.SJL-Ptprca Pepcb/BoyJ*) mice,
502 which subsequently generated *Vipr2*$^{-/-}$ CD45.1/2 mice and WT CD45.1 littermates.
503 Conditional VIPR2 knockout (*Vipr2*$^{fl/fl}$) mice were generated using CRISPR-Cas9
504 technology as described below. Mice in all experiments were 6–12 weeks old at the
505 starting point of treatments and all were colonized with SFB. All animal procedures were
506 performed in accordance with protocols approved by the Institutional Animal Care and
507 Usage Committee of New York University School of Medicine or the NIAID as
508 applicable.

509

510 *Generation of RORc(t)*^{Cre} *Vipr2*$^{fl/fl}$ *mice*

511 Mice carrying *loxP* sites flanking exons 3 and 4 of the Vipr2 gene (*Vipr2*$^{fl/fl}$) were generated
512 using published CRISPR/Cas9 protocols[38,39] at the NYU School of Medicine's Rodent Genetic
513 Engineering Laboratory. Briefly, guide RNAs targeting regions upstream of exon 3 (gRNA_16
514 sequence: GAAATCTCACAACAGATTCG) and downstream of exon 4 (gRNA_23 sequence:
515 TCTCCTCAGAAGCATCGAAT) were designed using the Crispr guide design
516 software (http://crispr.mit.edu/). gRNA recognition sequences were cloned into the pX330
517 vector (a gift from Dr. Feng Zhang, Addgene #42230), using oligos with a T7 promoter
518 containing the gRNA template that were chemically synthetized by IDT (Integrated DNA
519 Technologies). The products of PCR-amplified T7-gRNA were used as templates for in vitro
520 transcription (MEGAshortscript T7 kit, Thermo Fisher Scientific). The gRNAs were purified
521 using the MEGAClear Transcription Clean-up kit (Thermo Fisher Scientific). Two donor
522 templates (ssDNA_1 and ssDNA_2) with 200bp each were chemically synthetized by IDT. The
523 donor templates contained 60bp homology arms flanking a cassete containing a loxP
524 sequence and XhoI or SalI restriction sites, located in the original PAM sequence (mutated
525 PAM). Namely, ssDNA_1 (XhoI) for the region upstream exon 3:
526 (GGATGGCATTTACATAGGACCCCATCCCAGTGGCTGCTCAGAAGAGCACTCACTCCTTA
527 TCCctcgagataacttcgtataatgtatgctatacgaagttatCCGAATCTGTTGTGAGATTTCGAGAACTCATA
528 AGGACTGATAAGGCCACACAACTTGAGC), and ssDNA_2 for the region downstream exon 4
529 (TGATTTCTCCTAGGTCACACTCAGGGAGCATTTCCAGACACTGGAAAACTCCTGAGGCC
530 CgtcgacataacttcgtataatgtatgctatacgaagttatATTCGATGCTTCTGAGGAGACTATAATTAAACCC
531 TGCCTGTGTGAGGCATGGCTTCTGAT). Mice were generated by injection of a mixture of
532 mammalian optimized Cas9 mRNA (100 ng/µl, TriLink Biotechnologies), purified gRNA_16 and
533 gRNA_23 (50 ng/µl, each) and donor templates ssDNA_1 and ssDNA_2 (50ng/ul, each) in

534 injection buffer (10 mM Tris, pH 7.5; 0.1 mM EDTA) into the cytoplasm of C57BL/6J embryos in
535 accordance with standard procedures approved by the IACUC at the NYU School of
536 Medicine. Female CD-1 mice (Charles River) were used as foster mothers. F0 mice were
537 genotyped and sequenced (Sanger sequencing) to identify mice homozygous for both loxP
538 insertions. Founders bearing loxP insertions were then backcrossed at least one time to wild-
539 type C57BL/6J mice generating the *Vipr2*$^{fl/fl}$ mice. For the generation of *RORc(t)*^{Cre} *Vipr2*$^{fl/fl}$
540 mice, *Vipr2*$^{fl/fl}$ mice were crossed with *RORc(t)*^{Cre} mice for the generation of *RORc(t)*^{Cre} *Vipr2*$^{fl/fl}$
541 and *RORc(t)*^{Cre} *Vipr2*$^{+/+}$ littermates.
542
543 *VIPergic neuronal activation/inhibition using DREADDs*
544 To perform chemogenetic activation or inhibition of VIPergic neurons, we bred *VIP*$^{IRES\text{-}Cre}$
545 homozygous mice to *hM3Dq*$^{fl\text{-}stop\text{-}fl}$ mice (DREADD for activation) or *hM4Di*$^{fl\text{-}stop\text{-}fl}$ mice
546 (DREADD for inhibition), generating *VIP*$^{IRES\text{-}Cre}$*hM3Dq*$^{fl\text{-}stop\text{-}fl}$ (VIPergic activation) and *VIP*$^{IRES\text{-}}$
547 ^{Cre} *hM3Dq*$^{fl\text{-}stop\text{-}fl}$*hM4Di*$^{fl\text{-}stop\text{-}fl}$ mice (VIPergic inhibition). To perform 24h activation of the
548 DREADDs, mice were treated with Clozapine-N-Oxide (CNO, 1mg/Kg intraperitoneally,
549 TOCRIS) each 12h. Our experiments with *VIP*$^{IRES\text{-}Cre}$ only mice revealed that these dose of
550 CNO treatment does not affect ILC3 function. To perform activation of the DREADDs during
551 *Citrobacter rodentium* infection, mice were treated daily with CNO (1mg/Kg, intraperitoneally)
552 from day 1 to day 4 after infection.
553
554 *Food restriction protocol*
555 For a period of two weeks, food was made available to mice only for 12h per daily cycle. Mice
556 were kept in two different regimens: Dark-phase fed mice, with food being available between 6

557 PM – 6AM (ZT 12->ZT 0); and light-phase fed, with food being available between 6 AM – 6PM
558 (ZT 0->ZT 12). To avoid littering, at the beginning of the fasting period of each regimen, mice
559 were transferred to a clean cage containing alpha cellulose clean bedding
560 (Shepherd's™ALPHA-dri). Mice were provided with free access to water.
561
562 *Gavage of Liquid Test Diet*
563 Dry powder micro stabilized rodent liquid diet (Test Diet, LD 101) was blended (mechanical
564 blender) vigorously for 30 seconds in saline (NaCl 0.9%) at 0.5g/mL. Mice were gavaged with
565 400ul of this solution using a polyurethane feeding tube (16ga x 38mm, FTPU-16-38-50,
566 INSTECH) every 45 min for 6 h.
567
568 *Generation of bone marrow VIPR2$^{+/+}$/VIPR2$^{-/-}$ chimeric reconstituted mice*
569 Bone marrow mononuclear cells were isolated from CD45.1 *VIPR2*$^{+/+}$ and CD45.2 (or
570 CD45.1/2) *VIPR2*$^{-/-}$ mice by flushing the long bones. Red blood cells were lysed with ACK
571 Lysing Buffer and the remaining cells were resuspended in PBS for injection in at a 1:1 ratio
572 (WT:VIPR2 KO). 4×10^6 cells were injected intravenously into 6 week old CD45.1/2 (CD45.2)
573 mice that were irradiated 4h before reconstitution using 1000 rads/mouse (2x500rads, at an
574 interval of 3h, at X-RAD 320 X-Ray Irradiator). To deplete intestinal ILC3, one day after the
575 bone marrow transfer, mice were treated with InVivoMAb anti-mouse Thy1.2 (200ug/mice for 4
576 consecutive days, Clone 30H12, BioXCell). Experiments were performed 6-7 weeks after the
577 last treatment with α-Thy1.2.
578
579 *Radioactively labeled triglyceride absorption assay*

580 Plasma ^{3}H-CPM (counts per minute) was measured 1-4h after gavage with ^{3}H-Triolein–
581 containing lipid[40]. Briefly, mice were injected with poloxamer 407 (1g/Kg, i.p., Sigma,
582 #16758). After 30 minutes, mice were gavaged with a mixture of 2μCi ^{3}H-Triolein in
583 200ul of 20% intralipid oil emulsion. Blood samples were collected and diluted in Liquid
584 Scintillation Counting cocktail (Ultima Gold) and measured using a Scintillation counter
585 (Beta Counter MicroBeta^{2} System, Perkin Elmer).
586
587 *IL-22 in vivo Blockade*
588 For experiments with IL-22 blockade, mice were injected with monoclonal α-IL-22 (Clone 8E11,
589 250μg/mouse, generously provided by Tangsheng Yi, Genentech), 12 hours before sample
590 collection. Control groups received mIgG1 (inVivoMAb, BioXCell).
591
592 *C. rodentium mediated colon inflammation*
593 *C. rodentium* strain DBS100 (ATCC51459; American Type Culture Collection) was grown at
594 37°C in LB broth to OD600 reading between 0.5 and 0.7. *VIP$^{IRES\text{-}Cre}$hM3Dq$^{fl\text{-}stop\text{-}fl}$* (VIPergic
595 activation) and C57BL/6 mice were inoculated with 200 µl of a bacterial suspension (2×10^{9}
596 CFU) by oral gavage. *VIP$^{IRES\text{-}Cre}$ hM3Dq$^{fl\text{-}stop\text{-}fl}$hM4Di$^{fl\text{-}stop\text{-}fl}$* mice (VIPergic inhibition) and
597 *RORc(t)^{Cre} Vipr2$^{fl/fl}$* were inoculated with 200 µl of a bacterial suspension ($3\text{-}4\times10^{10}$ CFU) by
598 oral gavage. For DREADD experiments, CNO treatment started at 1 day post-infection (d.p.i.)
599 until 4 d.p.i. Mice were followed the next 12 days post-infection (d.p.i.) to measure survival
600 rate. At 9 d.p.i. fecal pellets were collected and the mice dissected to harvest spleen and liver.
601 Samples were weighted and minced on sterile deionized water with Triton 0.1% and filtered on
602 a 70μm cell strainer. The filtered samples were used to measure *C. rodentium* burden with

603 serial dilutions (triplicates) on MacConkey agar plates.

604

605 *Immunofluorescence and Confocal Microscopy*

606 Slide section staining: Small intestines from perfused SFB^{+} *Rorc*(t)$^{EGFP/+}$ or *VIP*$^{IRES-}$

607 ^{Cre}*tdTomato*$^{fl-stop-fl}$ mice were Swiss-rolled, fixed for 4h in 4% paraformaldehyde, incubated

608 overnight in 30% sucrose at 4°C, and frozen in embedding medium for frozen specimens

609 (O.C.T, Tissue-Tek, Sakura). Tissue was cut into 30-70 μM sections, blocked in PBST 0.5%

610 (0.5% Triton X-100, 10% normal donkey serum) for 1 h, and incubated overnight at 4°C using

611 the following antibodies: α-Vasoactive Intestinal Peptide (1:1000, rabbit polyclonal, 20077,

612 Immunostar), α-Tyrosine Hydroxilase (1:50, rabbit polyclonal, AB152, Millipore), α-Substance P

613 (1:3000, rabbit polyclonal, 20064 Immunostar), α-GFP Alexa Fluor 488 (1:500, clone: FM264G,

614 Biolegend), α-TCRβ Brilliant Violet 421 (1:50, Biolegend), α-β-3-Tubulin Alexa Fluor 594 or

615 Alexa Fluor 488 (1:500, clone:AA10, Biolegend). Tissue was washed and when needed

616 incubated with secondary fluorescently labeled antibodies (Donkey Anti-Rabbit Pacific Blue or

617 Alexa Fluor 647) for 2h before nuclear staining with Draq-7 (R&D Systems) or 4′,6-diamidino-2-

618 phenylindole (DAPI, ThermoFisher).

619 Whole mount stainings: Ileum was collected from perfused *VIP*$^{IRES-Cre}$*hM3Dq*$^{fl-stop-fl}$ mice, flat

620 opened and cleared of fecal material. The flat tissue was fixed overnight in 4%

621 paraformaldehyde at 4°C. Whole tissue was cut in sections of 4cm, blocked in PBST 0.5%

622 (0.5% Triton X-100, 10% normal donkey serum) overnigh at 4°C, and incubated for 48h at 4°C

623 using the following antibodies: α-HA Alea Fluor 647, for staining of HA-tagged hM3Dq,

624 (16B12, 1/300, Biolegend) and α-cFOS (1/100, 9F6, Rabbit, Cell, Signaling #2250). Tissue

625 was washed for 24h at 4°C and incubated with secondary fluorescently labeled antibodies

626 (Donkey Anti-Rabbit Alexa Fluor 488, Thermo Fisher) for 24h at 4°C. Tissue was washed for
627 24h before nuclear staining with 4′,6-diamidino-2-phenylindole (DAPI, ThermoFisher). Images
628 were acquired using a Zeiss LSM 710 confocal (Carl Zeiss). The imaging data were processed
629 and analyzed using Image J software (NIH, Bethesda, MD). Imaris software version 9.0.1
630 (Bitplane; Oxford Instruments) was used to generated reconstructed 3D images.
631
632 *Isolation of Lamina Propria Lymphocytes (LPLs) from the small intestine*
633 Whole small intestine, proximal small intestine (14cm), ileum (distal 14cm of the small
634 intestine) or the large intestine were dissected from mice. Unless indicated, all the dissections
635 were performed between ZT2-ZT3. Mesenteric fat tissue and Peyer's patches were carefully
636 removed from these tissues. Intestinal tissue was opened and extensively cleaned of fecal
637 matter. Following, this tissue was sequentially treated with HBSS 1X (1 mM DTT) at 37°C for
638 10 min with gentle shaking (200rpm), and twice with 5 mM EDTA at 37°C for 10 min to remove
639 epithelial cells. The EDTA fraction (ileal extracts enriched for IECs) was filtered using a 100uM
640 strainer, centrifuged and suspended in Trizol for further RNA isolation. The remaining tissue
641 was then minced with a scissor and dissociated in RPMI containing 10% FBS, Dispase (0.05
642 U/ml; Worthington), collagenase (1 mg/ml collagenase II; Roche) and DNase I (100 µg/ml;
643 Sigma) at constant shaking at 37°C for 45 min (175rpm). The digested tissue was then filtered
644 through a 70μm strainer to remove large debris. Viable Lamina Propria Lymphocytes (LPLs)
645 were collected at the interface of a 40%/80% Percoll/RPMI gradient (GE Healthcare).
646
647 *Isolation of ILC3, γδT17 and Th17 cells from the small intestine*
648 CCR6^{+} and CCR6^{neg} ILC3

649 (DAPI^{neg}CD3^{neg}CD11b^{neg}CD11c^{neg}CD14^{neg}CD19^{neg}TCRβ^{neg}TCRγ^{neg}NK1.1^{neg}KLRG1^{neg}CD127^{+}

650 CD90.2^{+}), γδT17

651 (DAPI^{neg}CD11b^{neg}CD11c^{neg}CD8^{neg}D14^{neg}CD19^{neg}NK1.1^{neg}TCRγ^{+}TCRβ^{neg}GFP^{+}CD3^{+}) and Th17

652 (DAPI^{neg}CD11c^{neg}CD8^{neg}CD14^{neg}CD19^{neg}NK1.1^{neg}TCRγ^{neg}TCRβ^{+}GFP^{+}CD3^{+}) were isolated

653 from small intestine of the BAC-transgenic *Rorc(t)-Gfp^{TG}* mice using the ARIA II FACS Sorter

654 (sorted through a 70μM nozzle, BD Biosciences) and resuspended in TRIZOL for further RNA

655 isolation. CCR6^{+} ILC3 were also isolated from *VIPR2$^{+/+}$/VIPR2$^{-/-}$* chimeric reconstituted mice

656 for further RNA isolation.

657

658 *ILC3 in vitro cell culture*

659 CCR6^{+} and CCR6^{neg} ILC3

660 (DAPI^{neg}CD3^{neg}CD11c^{neg}CD14^{neg}CD19^{neg}TCRβ^{neg}TCRγ^{neg}NK1.1^{neg}KLRG1^{neg}CD127^{+}CD90.2^{+})

661 were isolated from small intestine LPLs of C57BL/6 mice using the ARIA II FACS Sorter (BD

662 Biosciences). ILC3 were cultured at 37°C in flat bottom 96 well plates (10^{4} cells/well) in RPMI

663 supplemented with 10% heat-inactivated FBS (Hyclone), 50 U penicillin-streptomycin

664 (Hyclone), 2 mM glutamine (Hyclone), 10mM HEPES (Hyclone), 1mM sodium pyruvate

665 (Hyclone) and 50 μM β-mercaptoethanol (Gibco). ILC3 were stimulated with IL-23 (100-300

666 pg/mL, R&D systems) and/or VIPR2 ligands (BAY-559837: 1-100nM, and VIP: 1nM-1uM,

667 TOCRIS) for 16h (37°C), washed, incubated in for 4h at 37°C in RPMI with 10% FBS, phorbol

668 12-myristate 13-acetate (PMA) (50 ng/ml; Sigma), ionomycin (500 ng/ml;Sigma) and Golgi

669 Plug (BD Bioscience), and stained for membrane extracellular markers in Staining Buffer (PBS

670 FBS 2% EDTA 5mM) and for intracellular markers using Cytofix/Cytoperm buffer set following

671 manufacturer's protocol (BD Biosciences). Acquisition of cytometric parameters was

672 performed on an LSRII (BD Biosciences). All data were analyzed using FlowJo Software
673 Version 10 (Tree Star).
674
675 *Antibodies for intracellular staining and flow cytometry*
676 Single cell suspensions were pelleted and resuspended with surface-staining antibodies in
677 PBS FBS 2% EDTA 1mM. Staining was performed for 20-30min on ice. Live/dead fixable blue
678 (ThermoFisher) was used to exclude dead cells. The following monoclonal antibodies were
679 purchased from eBiosciences, BD Pharmingen or BioLegend: CD3, CD45.1, CD45.2, TCRβ,
680 CD11c, CD14, CD19, KLRG1, TCRγ, RORγ/γt, NK1.1, CD127, CD90.2, CCR6, Sca-1, IL17A
681 and IL-22. Analysis of ex-vivo cytokine production in ILC3 was performed in unstimulated cells
682 (unless indicated), with LPLs incubated for 4h at 37C in RPMI with 10% FBS and GolgiPlug
683 (BD). Cells were then stained for surface markers and anti-CD16/anti-CD32 before fixation and
684 permeabilization, and then subjected to intracellular cytokine staining for IL-22 and IL-17A
685 according to the manufacturer's protocol (Cytofix/Cytoperm buffer set from BD Biosciences).
686 For analysis of ex-vivo cytokine production by Th17/γδT17 cells were incubated for 4 hours at
687 37C in RPMI with 10% FBS, phorbol 12-myristate 13-acetate (PMA) (50 ng/ml; Sigma),
688 ionomycin (500 ng/ml;Sigma) and GolgiStop (BD). After surface and live/dead staining, cells
689 were treated using the the FoxP3 staining buffer set from eBioscience according to the
690 manufacturer's protocol. Intracellular stains were prepared in 1X eBioscience permwash buffer
691 containing anti-CD16/anti-CD32, normal mouse IgG (conc), and normal rat IgG (conc).
692 Staining was performed for 30-60min on ice. Flow cytometric analysis was performed on an
693 LSR II (BD Biosciences) or an Aria II (BD Biosciences) and analyzed using FlowJo software
694 version 10 (Tree Star).

695

696 *Blood collection*

697 Peripheral and portal vein blood were collected under general anesthesia (Ketamine
698 100mg/Kg, Xylazine 15mg/Kg). Peripheral blood was collected through orbital venous plexus
699 bleeding with a glass capillary in a tube containing EDTA (25mM) as an anticoagulant. Plasma
700 was collected after centrifugation of the collected sample and frozen until processing. Surgery
701 was performed to collect blood from the portal vein, which drains the gastrointestinal tract.
702 Briefly, after laparotomy, the portal vein was localized and the blood was collected with a
703 syringe. Portal vein blood was processed following the same protocol above for peripheral
704 blood.

705

706 *Evaluation of villi and crypt morphology in the small intestine*

707 Small intestine samples (14 cm distal from the pylorus, 10cm long) were gently swiss rolled
708 from the distal end and fixed in 4% paraformaldehyde (Electron Microscopy Science, Hatfield
709 USA). Formalin-fixed tissues were then processed for paraffin embedding, cut into 5-micron
710 thick sections and stained with hematoxylin and eosin (H&E) or Ki-67/hematoxylin as per
711 protocol by the Experimental Pathology Core Laboratory at New York University (NY, USA).
712 Measurement of villi and crypt length on H&E slides was performed by two independent
713 researches in a blinded fashion using coded slides. Per sample, we analyzed a total of 6 slides
714 with a distance of 100uM between each cut. For each slide, 10 villi/crypts were measured, as a
715 total of 60/sample. The mean values of villi and crypt length were plotted. The imaging data
716 were processed and analyzed using Image J software (NIH, Bethesda, MD). Quantification of
717 frequency of Ki-67+ cells in the whole crypt region was performed in a blinded fashion using

718 coded slides and the tools of Qupath software[41].

719

720 *Tissue processing for ELISA*

721 Distal Ileum (6 cm from the ileal-cecal junction) was collected and extensively washed to clean
722 out fecal matter. The samples were weighed and, using a tissue homogenizer, extracted in
723 PBS Tween 0.1% (with protease inhibitor) and centrifuged to remove tissue debris. The
724 supernatant was frozen until measurement of VIP concentrations in the tissue.

725

726 *ELISA for Vasoactive Intestinal Peptide*

727 VIP content was measured in the blood plasma or homogenized tissue following
728 manufacturer's recommendations (EIAM-VIP-1, RayBiotech).

729

730 *Measurement of plasma concentration of triglycerides*

731 Peripheral blood was collected as described above and plasma was used to quantify
732 triglyceride concentrations following manufacturer's recommendations (Sigma-Aldrich,
733 MAK266).

734

735 *Scanning Electron Microscopy*

736 Scanning Electron Microscopy was performed on 1-1.5 cm pieces from terminal ileum
737 (2cm above the ileal-cecal junction). Intestine was cut open and washed to remove fecal
738 matter, pinned in dental wax and fixed for 2h with a 0.1M sodium cacodylate buffer (CB,
739 pH 7.4) containing 2.5% glutaraldehyde and 2% paraformaldehyde. Samples were post
740 fixed in 1% OsO4 for 2 hours, dehydrated in ethanol, and critical point dried using

741 Tousimis autosamdsri 931 (Rockwille, MD). The dried intestines were put on SEM
742 stabs, sputter coated with gold/palladium by DESK V TSC HP Denton Vacuum
743 (Moorestown, NJ), and images were taken on random locations in the tissue by Zeiss
744 Gemini300 FESEM using secondary electron mode at 5kv. For quantification of SFB
745 length, random fields were selected for measurement using Image J.
746
747 *RNA extraction from intestinal epithelial cells, RT-PCR and qPCR*
748 RNA isolation of CCR6^{+} ILC3, CCR6^{neg} ILC3, γδT17, Th17 and ileal epithelial cells, was
749 performed using TRIzol following manufacter's instructions (Invitrogen) followed by
750 DNase I (Qiagen) treatment and cleanup with RNeasy MinElute kit (Qiagen) following
751 manufacturer protocols. cDNA was generated using SuperScriptTM IV First-Strand
752 Synthesis System (ThermoFisher). Gene-specific primers spanning exons were used:
753 *Rps17* (F:'5-cgccattatccccagcaag-3'/ R:'5-tgtcgggatccacctcaatg-3'), *RegIIIγ* (F:'5-
754 tctgcaagacagacaagatgct-3'/ R:'5-ggggcatctttcttggcaac-3'), *Fabp2* (F:'5-
755 gtctagcagacggaacggag-3'/R:'5-ctccttcatatgtgtaggtctgga-3'), *Cd36* (F:'5-
756 tggccttacttgggattgg-3'/R:'5-ccagtgtatatgtaggctcatcca-3'). Quantitative PCR was
757 performed using the Hot Start-IT SYBRGreen (Affymetrix) on the Roche real-time PCR
758 system (Roche 480). Values were normalized to *Rps17* gene for each sample. For
759 evaluation of *Vipr2* mRNA expression, TaqMan probes *for Vipr2* (Mm01238618) and
760 *Hprt* (Mm00446968) were purchased from Thermo Fisher Scientific and reactions were
761 run with the CFX Connect Real—Time PCR Deterction System (Bio-Rad).
762
763 *Analysis of microbiota composition in the ileal fecal material, fecal pellet and ileal tissue*

764 The ileum (ileal tissue: 1 cm), ileal fecal content, fecal pellet were collected from mice,
765 and bacterial DNA was extracted with the QIAamp DNA Stool Kit (QIAGEN) following
766 the manufacturer's instructions. In the ileal tissue, SFB was quantified by qPCR with
767 primers specific for 16S SFB rRNA genes (SFB F- sequence/SFB R- sequence)using
768 Hot Start-IT SYBRGreen (Affymetrix) on the Roche real-time PCR system (Roche 480).
769 The relative values of SFB in the tissue were normalized based on the amounts of host
770 gDNA using primers specific for the genomic *Hif1a* locus (Hif1a F-sequence / Hif1a R-
771 sequence). In the ileal fecal content and fecal pellet, SFB was quantified by qPCR with
772 primers specific for SFB and the relative values were normalized based on the total
773 relative amounts of 16S rDNA (16S F-sequence / 16S R-sequence).
774 For analysis of the whole microbial community composition in the ileal and fecal matter,
775 sequencing of the 16S rRNA was performed as previously described[42] in a MiSeq
776 instrument (Ilumina, San Diego, USA) using 150bp, paired ended chemistry. 16S rRNA
777 sequence data were processed using QIIME v2[43].
778
779 *Data processing of publicly available RNA-seq*
780 DESeq2-normalized gene quantification and differential expression analysis were downloaded
781 from GSE116092[16]. Raw counts were downloaded from GSE127267 (ImmGen ULI RNA-seq
782 data)[17] and differential expression analysis was performed using DESeq2. Normalized counts
783 were used for downstream analysis. A cutoff was made based on the normalized counts of a
784 known non-expressed gene (*Foxp3*) (GSE116092, cut-off $\leq$ 9 and for GSE127267, cutoff <25)..
785 GO term analysis of GSE116092[16] was done using g:Profiler. For heat maps, genes were
786 considered differentially expressed with FDR < 0.01 and log2 fold change $\geq$ 2.

Library preparation for RNA sequencing and transcriptomic analysis

RNA-seq libraries for CCR6^{+} ILC3 were prepared with the TruSeq Stranded Total RNA Library Prep Gold Kit (Illumina, 20020598). The sequencing was performed using Illumina NextSeq instrument (Ilumina, San Diego, USA) using 150bp, paired ended chemistry. RNA-seq libraries were prepared and sequenced by the Genome Technology Core at New York University School of Medicine. Fastq files were aligned to the mouse Ensemble genome GRCm38 with STAR v 2.6.1d. Read pairs were counted using featurecounts from the Subread package v 1.6.2, prior to normalization and differential expression analysis which were performed using DESeq2 (Wald test with Benjamini–Hochberg correction to determine the FDR). Genes were considered differentially expressed with FDR<0.05 and log2 fold change > 1. Gene pathways and functions were assessed using Ingenuity Pathway Analysis (Qiagen Bioinformatics).

Statistical analysis

Unpaired two-sided *t-test*, paired two-sided *t-test,* one-way ANOVA with multiple comparisons with Bonferroni correction, two-way ANOVA with multiple comparisons and Bonferroni correction, Mann-Whitney test, Mantel Cox test (for survival curves), were performed to compare the results using GraphPad Software Version 8 (GraphPad Software). No samples were excluded from analysis. We treated less than 0.05 p value as significant：$*P < 0.05$, $**P < 0.01$, $***P < 0.001$, and $****P < 0.0001$.

810 **EXTENDED DATA FIGURE LEGENDS**

811

812 **Extended Data Figure 1. Enrichment of transcripts related to nervous system/neural**
813 **functions and development in CCR6^{+} ILC3. a,** Volcano-plot of differentially expressed genes
814 between CCR6^{+} ILC3 and CCR6^{neg} ILC3 isolated from the small intestine of C57BL/6 mice
815 GSE116092[16]. Green: Neurotransmitter/neuropeptide receptors, Blue: genes related to
816 nervous system development/axonal guidance and contact. **b,** Top 10 Gene-Ontology terms
817 from a comparison between subtypes of ILC3 showing enrichment of transcripts related to
818 neuron differentiation and generation in CCR6^{+} ILC3 when compared to CCR6^{neg} ILC3. Green:
819 Neurotransmitter receptors, Blue: genes related to nervous system development/axonal
820 guidance and contact. **c,** Vocano-plot of differentially expressed genes between CCR6^{+} ILC3
821 (enriched in cryptopatches and ILFs[44]) and NKp46^{+} ILC3 (low presence in CPs and ILFs[45])
822 (GSE127267[17]).

823

824 **Extended Data Figure 2. Cryptopatch-associated enteric neurons are also present in the**
825 **large intestine (colon) lamina propria. a, b** Representative immunofluorescence images of
826 lamina propria neuronal projections of enteric neurons in the large intestine of *Rorc(t)*$^{EGFP/+}$
827 mice. **(a)** Cluster of ILC3 (GFP^{+} cells, green) in close proximity of neuronal projections (βIII-
828 Tubulin, red) of the enteric neurons in the colon lamina propria. **(b)** Cluster of ILC3 (GFP^{+}
829 cells, blue) in close proximity of neuronal projections (βIII-Tubulin, red) of Vasoactive Intestinal
830 Peptide^{+} enteric neurons (green) in the colon lamina propria.

831

832 **Extended Data Figure 3.** Neurochemical code of the cryptopatch-associated enteric neurons

833 in the small intestine lamina propria. a-c, Representative immunofluorescence images of
834 different subtypes of lamina propria neuronal projections of enteric neurons in the small
835 intestine of *Rorc(t)*$^{EGFP/+}$ mice. (a) Substance P (green) is not present in neuronal projections
836 (βIII-Tubulin, red) localized inside CPs/ILFs (cluster of GFP^{+} cells, blue) in the lamina propria.
837 Representative of 15 CPs/ILFs analyzed in the small intestine of 4 different *Rorc(t)*$^{EGFP/+}$ mice).
838 No colocalization of substance P was observed in any of the cryptopatch associated neuronal
839 fibers. (b) Tyrosine hydroxylase^{+} neurons (green) are in close proximity but are not
840 represented among neuronal projections (βIII-Tubulin, red) localized inside CPs/ILFs (cluster of
841 GFP^{+} cells, blue) in the lamina propria. Representative of 20 CPs/ILFs analyzed in the small
842 intestine of 4 different *Rorc(t)*$^{EGFP/+}$ mice. TH^{+} fibers are found in proximity to ILC3 clusters but
843 never intercalate with CPs/ILFs. (c) Vasoactive Intestinal Peptide^{+} (green) neurons (βIII-
844 Tubulin, red) are in close proximity and interacting with ILC3 (GFP^{+}, blue) in CPs/ILFs.
845 Representative of 40 CPs/ILFs analyzed in the small intestine of 4 different *Rorc(t)*$^{EGFP/+}$ mice.
846

847 **Extended Data Figure 4. VIP agonist inhibits *in vitro* IL-22 production by**
848 **CCR6^{+}ILC3. a,** *Vipr2* mRNA expression (relative to *Hprt*) in different subtypes of RORγt^{+}
849 intestinal lymphoid cells, including ILC3 subsets, αβTh17 and γδT17 cells. RNA was
850 isolated from CCR6^{+} ILC3, CCR6^{negative} ILC3, Th17 (αβ RORγt^{+}T cells) and γδT17 (γδ
851 RORγt^{+}T cell) sorted from small intestine of *Rorc(t)*-Gfp^{TG} mice on basis of following
852 markers: γdT17 cells (Lin^{neg}RORgt^{GFP+}CD3^{+}TCRγ^{+}), αβT17
853 (Lin^{neg}RORγt^{GFP+}CD3^{+}TCRβ^{+}), CCR6^{+}ILC3 (Lin^{neg}RORγt^{GFP+}CD3^{neg} CCR6^{+}) and
854 CCR6^{neg}ILC3 (Lin^{neg}RORγt^{GFP+}CD3^{neg}CCR6^{neg}) (n=4 mice). N.D= not detected. **b)**

855 FACS plot showing gating strategy for identification and isolation of CCR6^{+} or CCR6^{neg}

856 ILC3 (DAPI^{neg}Lin^{neg} CD127^{+} CD90.2^{+}). **c, d,** *In vitro* activation of VIPR2 alone does not

857 induce cytokine production or activation of CCR6^{+} ILC3. Representative FACS plots **(c)**

858 and summary **(d)** for surface Sca-1 expression and intracellular IL-22 in small intestine

859 lamina propria CCR6^{+} ILC3. N= 3, representative of 2 independent experiments. **e,** *In*

860 *vitro* activation of VIPR2 promotes concentration-dependent inhibition of cytokine

861 production by CCR6^{+} ILC3. Summary for IL-22 and IL-17a intracellular expression in

862 small intestine lamina propria CCR6^{+} ILC3 stimulated *in vitro* for 12h with IL-23

863 (300pg/mL) with different concentrations of VIP. **P=< 0.05 ****P=< 0.001* (One-way

864 ANOVA). Data are representative of two independent experiments. **f,** *In vitro* activation

865 of VIPR2 does not reduce IL-23-induced Sca-1 expression on CCR6^{+} ILC3. Summary of

866 Sca-1 expression in small intestine lamina propria CCR6^{+} ILC3 stimulated *in vitro* for

867 12h with IL-23 (100pg/mL) with/without the VIPR2 ligands BAY-559837 or VIP. N=

868 3/group, representative of 2 independent experiments. **g, h,** *In vitro* VIPR2 activation

869 does not affect IL-23-induced IL-22 production by CCR6^{neg} ILC3. Representative FACS

870 plots **(g)** and summaries **(h)** of surface Sca-1 expression and intracellular IL-22 in small

871 intestine lamina propria CCR6^{neg} ILC3 stimulated *in vitro f*or 12h with IL-23 (100pg/mL)

872 with/without combination with VIPR2 ligand BAY-559837 (1nM). N= 3, and data are

873 representative of two independent experiments.

874

875 **Extended Data Figure 5. VIPR2 is required for *in vivo* inhibition of IL-22**

876 **production by CCR6^{+}ILC3. a, b,** Mixed bone marrow chimeras, showing **(a)** no

877 difference in frequency and ratio of WT (*Vipr2*$^{+/+}$) vs VIPR2 KO (*Vipr2*$^{-/-}$) CCR6^{+}ILC3 in
878 the ileum of mice receiving equal number of cells (N=17 mice, combined from 2
879 independent experiments) and **(b)** VIPR2-dependent inhibition of IL-22 production in
880 WT (*Vipr2*$^{+/+}$, CD45.1) versus VIPR2 KO (*Vipr2*$^{-/-}$, CD45.2) CCR6^{+} ILC3 in the ileum of
881 chimeric mice. N=11, ****P<0.0001 (*paired t-test*). Data are representative of two
882 independent experiments. **c, d, e,** Transcriptomic profile showing differences between
883 CCR6^{+} ILC3 among WT and VIPR2 KO isolated from mixed bone marrow chimeras. **(c)**
884 Volcano plot and **(d)** heatmap of selected genes differentially expressed between
885 CCR6^{+} ILC3 from *Vipr2*$^{+/+}$ and *Vipr2*$^{-/-}$ (FDR 5%, FC>1). **(e)** Analysis of pathways
886 associated with genes upregulated in *Vipr2*$^{-/-}$ CCR6^{+} ILC3 compared to *Vipr2*$^{+/+}$ CCR6^{+}
887 ILC3. **f, g,** Inactivation of *Vipr2* in ILC3 and T cells (*RORc(t)*^{Cre}*Vipr2*$^{fl/fl}$*)* does not affect **(f)**
888 proportion or **(g)** number of CCR6^{+} ILC3 in the mouse ileum. *RORc(t)*^{Cre}*Vipr2*$^{+/+}$: N=8;
889 *RORc(t)*^{Cre}*Vipr2*$^{fl/fl}$: N=6. **h, i** Inactivation of *Vipr2* (*RORc(t)*^{Cre}*Vipr2*$^{fl/fl}$*)* affects the
890 frequency of IL-22 production in CCR6^{+} ILC3. Representative FACS plot **(h)** and
891 summaries **(i)** indicating frequency of IL-22 production in CCR6^{+} ILC3 from the ileum of
892 *RORc(t)*^{Cre}*Vipr2*$^{+/+}$(N=8) and *RORc(t)*^{Cre}*Vipr2*$^{fl/fl}$ (N=6) mice. ***P<0.001 (*t-test*),
893 representative of 3 independent experiments.**j, k,** Inactivation of *Vipr2* promotes a minor
894 increase in the production of IL-17a in CCR6^{+} ILC3. Representative FACS plot **(j)** and
895 summaries **(k)** indicating frequency of IL-22 production in CCR6^{+} ILC3 from the ileum of
896 *RORc(t)*^{Cre}*Vipr2*$^{+/+}$(N=3) and *RORc(t)*^{Cre}*Vipr2*$^{fl/fl}$ (N=3) mice. Representative of three
897 independent experiments. **l, m,** Inactivation of *Vipr2* does not affect IL-17a or IL-22
898 production in CD3^{+}RORγt^{+} lymphoid populations, namely CD3^{+} RORγt^{+}TCRγ^{+}TCRβ^{neg}

899 (γδT17) and CD3^{+} RORγt^{+}TCRγ^{neg}TCRβ^{+} (Th17) cells. *RORc(t)*^{Cre}*Vipr2*$^{+/+}$(N=4) and

900 *RORc(t)*^{Cre}*Vipr2*$^{fl/fl}$ (N=4) mice. Representative of two independent experiments. FACS

901 plot **(l)** and summaries **(m)** indicating frequency of IL-17 and IL22. N.S: not significant.

902 **n, o,** Intestinal villi and crypt morphology (H&E) indicating the measurement of villi (red

903 bracket) and crypt (green bracket) lengths. Values represent the average length of 60

904 structures (villi or crypt) per mouse, in a 10cm region, starting 15cm from the pylorus.

905 *P<0.05 and **P<0.01 (*t-test*). *RORc(t)*^{Cre}*Vipr2*$^{+/+}$(N=4) and *RORc(t)*^{Cre}*Vipr2*$^{fl/fl}$ (N=3)

906 mice. **p, q,** Ki-67 and Haematoxilin staining, revealing increased Ki-67^{+} cells in the crypt

907 region of the small intestine (automated counting). **P<0.01 (*t-test*),

908 *RORc(t)*^{Cre}*Vipr2*$^{+/+}$(N=4) and *RORc(t)*^{Cre}*Vipr2*$^{fl/fl}$ (N=3) mice.

909

910 **Extended Data Figure 6. Effect of VIPergic neuronal modulation with DREADDs on IL-22**

911 **production by CCR6^{+} ILC3. a, b,** *VIP*^{Cre} activity in neurons in the gut. Homozygous *VIP*^{Cre}

912 mice were bred to homozygous *Rosa26*$^{fl\text{-}st\text{-}fl\text{-}tdTomato}$. **(a)** Distribution of tdTomato^{+} projections in

913 the small intestine lamina propia. tdTomato: red; nucleus/Dapi: blue. **(b)** tdTomato positive and

914 negative neurons present in the small intestine. tdTomato: red; pan=neuronal marker β3-

915 tubulin: green. Two distinct β3-tubulin^{+} tdTomato^{+} neuronal projections (white arrows) can be

916 observed in a bundle of enteric neurons in the villi. Yellow: β3-tubulin^{+} tdTomato^{negative}

917 projection. **c,** Nuclear cFOS localization in VIPergic neurons 2h after CNO (1mg/Kg, i.p.) or

918 vehicle treatment of mice expressing the DREADD for activation under the control of *VIP*^{Cre}

919 (VIP^{Cre} hM3Dq$^{fl/+}$). cFOS-AF488: red, hM3Dq-TA-AF647: green, Nucleus/Dapi: blue. **d, e, f,**

920 Effect of chemogenetic modulation of VIPergic neurons on IL-22 production by CCR6^{+} ILC3 in

921 the small intestine (S.I.) and large intestine (L.I.). Representative FACS plot **(d)** and summaries
922 of IL-22 production by $CCR6^{+}$ ILC3 in mice expressing the DREADD for inhibition (hM4Di) **(e)**
923 and for activation (hM3Dq) **(f)**. All the mice were treated with CNO (1mg/Kg, i.p, twice, 24h
924 before sample collection). **(e):** N= 6 mice/group; **(f)** VIP^{Cre}: N= 6, $VIP^{Cre}hM3Dq^{Cre}$: N= 5.
925 *P<0.05, ****P<0.001 (*t-test*). **g, h,** No difference in the frequencies of IL-17 and IL-22
926 production by $CD3^{+}$ $ROR\gamma t^{+}TCR\gamma^{+}TCR\beta^{neg}$ ($\gamma\delta$T17) and $CD3^{+}$ $ROR\gamma t^{+}TCR\gamma^{neg}TCR\beta^{+}$ (Th17)
927 cells after activation of VIPergic neurons. Representative FACS plot **(g)** and summaries **(h).**
928 All the mice were treated with CNO (1mg/Kg, i.p, twice, 24h before sample collection).
929
930 **Extended Data Figure 7. VIPergic neurons regulate host resistance to enteropathogenic**
931 ***Citrobacter rodentium*. a,** Normalized *Vip* mRNA expression in the large intestine (cecum
932 and proximal colon) of C57BL/6 mice at different time points after oral infection with *Citrobacter*
933 *rodentium* ($2x10^{9}$ CFU). **Day** 0: N=4; 2, 4 and 9 days after infection: N=6. *P<0.05 compared to
934 day 0 (one-way ANOVA), representative of two independent experiments**. b, c,** Increased VIP
935 activity in the gastrointestinal tract but not systemically in mice infected with *C. rodentium.*
936 Concentrations of VIP in plasma from the (**b**) hepatic portal vein, which drains the
937 gastrointestinal tract, and (**c**) peripheral blood of mice at different time points after intragastric
938 administration of vehicle or *C. rodentium* ($2x10^{9}$ CFU). d.p.i: days post-intragastric infection
939 with *C. rodentium*. Data shown are pooled from two independent experiments. N= 8/group,
940 *P<0.05, ****P<0.0001(*t-test*). **d,** Off -target effects of CNO treatment do not account for
941 mortality observed using activating DREADD during *C. rodentium* infection**.** Survival rates for
942 *C. rodentium*-infected $Vip^{IRES\text{-}Cre}$ *or* $Vip^{IRES\text{-}Cre}hM3Dq^{fl\text{-}stop\text{-}fl/+}$ mice treated with CNO (1mg/Kg,
943 daily, 1-4 d.p.i.: yellow rectangle). Vehicle: n=11, CNO: n=9. **e, f,** Infectious burden in feces of

944 (**e**) *Vip*$^{IRES\text{-}Cre}$*hM3Dq*$^{fl\text{-}stop\text{-}fl/+}$ (activating DREADD) and (**f**) *Vip*$^{IRES\text{-}Cre}$*hM4Di*$^{fl\text{-}stop\text{-}fl/+}$ (inhibitory

945 DREADD) mice treated with vehicle or CNO (1mg/Kg, daily, 1-4 days post-intragastric infection

946 with $2x10^9$ CFU for *Vip*$^{IRES\text{-}Cre}$*hM3Dq*$^{fl\text{-}stop\text{-}fl/+}$ and $4x10^{10}$ CFU for *Vip*$^{IRES\text{-}Cre}$*hM4Di*$^{fl\text{-}stop\text{-}fl/+}$ mice).

947 Log_{10} Colony Forming Units (CFU) of *C. rodentium* 9 days post-oral innoculation (9 d.p.i.).

948 Data representative of two independent experiments. Activating DREADD mice: Vehicle: n=11,

949 CNO: n=9. Inhibitory DREADD mice: Vehicle: n=8, CNO: n=7**,** **P*=0.0009 (Mann-Whitney test).

950 **g, h,** Exogenous treatment with recombinant murine IL-22 (rmIL-22, 250μg/mouse/day)

951 protects against increase in **(g)** mortality and **(h)** bacterial dissemination to the spleen induced

952 by VIPergic activation of *Vip*$^{IRES\text{-}Cre}$*hM3Dq*$^{fl\text{-}stop\text{-}fl/+}$mice. ***P=0.0321 (Mantel Cox test,* survival);

953 ***P*=0.0022 *(*Mann-Whitney test). For visualization in the logarithm scale (e-g), CFU counts of

954 0 were attributed a value of 1. **i, j,** Inactivation of *Vipr2* expression in ILC3 (*RORc(t)*^{Cre}*Vipr2*$^{fl/fl}$*)*

955 enhances barrier protection after oral infection with the enteropathogen *C. rodentium* ($3x10^{10}$

956 CFU) **(i)** Discrete protection for weight loss in the first 9 days after infection. **(j,)** Log_{10} Colony

957 Forming Units (CFU) of *C. rodentium* 9 days post-oral inoculation with $3x10^{10}$ CFU.

958 *RORc(t)*^{Cre}*Vipr2*$^{fl/fl}$ mice display reduced amounts of *C. rodentium* translocation to the spleen

959 and liver, and reduced CFU counts in the feces**.** *RORc(t)*^{Cre}*Vipr2*$^{+/+}$(N=10) and

960 *RORc(t)*^{Cre}*Vipr2*$^{fl/fl}$ (N=10) mice. **P*<0.05, ***P*<0.01 ****P*<0.001, ****P*<0.0001, [two-way ANOVA

961 **(i)** and Mann-Whitney test **(j)**]. For visualization in the logarithm scale (e-g), CFU counts of 0

962 were attributed a value of 1.

963

964 **Extended Data Figure 8. Feeding controls intestinal VIP release and IL-22**

965 **production by CCR6$^+$ ILC3 via activation of VIPR2. a,** Measurement of concentration

966 of VIP in the ileum reveals higher amounts during dark-phase (feeding period, ZT12-
967 ZT0) than in the light-phase (resting period, ZT0-ZT12). N=4, representative of two
968 independent experiments. **b,** Concentrations of VIP in plasma isolated from hepatic
969 portal vein blood of mice fed or fasted for 6 h. Blood samples were collected at two
970 different time-points, during the light-phase period (ZT 6, 12PM) and the dark-phase
971 period (ZT 18, 12AM). N=4, *P<0.05; **P<0.01 (*t-test*). **c,** Concentrations of VIP in
972 plasma isolated from the peripheral blood of mice. Blood samples were collected at two
973 time-points, during the light-phase period (ZT 6, 12PM) and the dark-phase period (ZT
974 18, 12AM). N=4, representative of two independent experiments. **d,** IL-22 expression by
975 $CCR6^{+}$ ILC3 from the ileum of CD45.1 *Vipr2*$^{+/+}$:CD45.2 *Vipr2*$^{-/-}$ bone marrow chimeric
976 mice at 6h after fasting (fasted, ZT 6) and 6h after feeding (fed, ZT 18). n=7/group,
977 **P<0.01 (*paired t-test*). Data are representative of two pooled independent
978 experiments. **e,** Ratio of IL-22-expressing cells, relative to Figure 3c, among $CCR6^{+}$
979 ILC3 from the ileum of CD45.1 *Vipr2*$^{+/+}$:CD45.2 *Vipr2*$^{-/-}$ bone marrow chimeric mice at
980 6h after fasting (Fasted, ZT 6) and 6h after feeding (Fed, ZT 18). n=7, ***P<0.001 (*t-*
981 *test*).
982
983 **Extended Data Figure 9. Feeding/fasting modulates growth of epithelium-**
984 **associated segmented filamentous bacteria (SFB) and composition of fecal**
985 **commensal microbiota. a,** Representative SEM images (magnifications: 1K, upper
986 pannel, and 3K, lower pannel) showing epithelial-attached SFB in the ileum of mice 12 h
987 after feeding (long filaments) or fasting (short-filaments, “stubbles”) at ZT 0. **b,** SFB
988 lengths at different time points during the day in mice that had been fed for two weeks

989 during the light-phase (Light-phase fed: ZT0 to ZT12, red) or during the dark-phase
990 (dark-phase fed: ZT12 to ZT0, blue). **c,** Relative amounts (log) of SFB 16S measured in
991 the ileal tissue by qPCR, normalized based on host genomic DNA quantity. Mice were
992 fed for two weeks during the light-phase or during the dark-phase and the ileal tissue
993 was collected at two different time points, ZT0 or ZT12. **d,** Weighted Unifrac Principal
994 coordinate analysis of 16S rRNA composition in the fecal pellet of mice that had been
995 fed for two weeks during the light-phase (circles) or during the dark-phase (diamonds).
996 Fecal samples were collected from the same mice at different time points (ZT0 or
997 ZT12). Dark-phase fed: at ZT0 these mice had been fed for 12h (red diamond), while at
998 ZT12 they had fasted for 12h (blue diamond); Light-phase fed: at ZT0 these mice had
999 fasted for 12h (blue circle), while at ZT12 they had been fed for 12h (red circle). **e,**
1000 Phylogenetic profile of the fecal microbiota composition associated with feeding/fasting
1001 status in the fecal pellet of mice that had been fed for two weeks during the light-phase
1002 or during the dark-phase.
1003

1004 **Extended Data Figure 10. Loss of *Vipr2* expression in ILC3 (*RORc(t)*^{Cre}*Vipr2*$^{fl/fl}$**
1005 **mice) affects the growth of epithelium-associated SFB and the composition of**
1006 **ileal and fecal commensal microbiota. a,** Relative amounts (log) of SFB 16S
1007 measured in the ileal tissue from *RORc(t)*^{Cre} *Vipr2*$^{+/+}$ or *RORc(t)*^{Cre} *Vipr2*$^{fl/fl}$ mice (male,
1008 8 weeks old) that had been fed for two weeks during the dark-phase. Samples were
1009 collected at ZT0 (12h fed). qPCR, normalized based on host gDNA levels. This cohort is
1010 composed of 3 different pairs of *RORc(t)*^{Cre} *Vipr2*$^{+/+}$ and *RORc(t)*^{Cre} *Vipr2*$^{fl/fl}$ littermates,
1011 housed in 3 different cages. **b,** Weighted Unifrac Principal coordinate analysis (PCoA) of

1012 16S rRNA composition in the ileal fecal material from *RORc(t)*^{Cre} *Vipr2*$^{+/+}$ or *RORc(t)*^{Cre}
1013 *Vipr2*$^{fl/fl}$ mice (male, 8 weeks old) that had been fed for two weeks during the dark-
1014 phase. Samples were collected at ZT0 (12h fed). This cohort was composed of 3 pairs
1015 of *RORc(t)*^{Cre} *Vipr2*$^{+/+}$ and *RORc(t)*^{Cre} *Vipr2*$^{fl/fl}$ littermates, housed in 3 different cages.
1016 **c,** Phylogenetic profile of the microbiota composition in the ileal fecal material of
1017 *RORc(t)*^{Cre} *Vipr22*$^{+/+}$ or *RORc(t)*^{Cre} *Vipr2*$^{fl/fl}$ mice after 12h of feeding. **d,** Weighted
1018 Unifrac Principal coordinate analysis (PCoA) of 16S rRNA composition in fecal pellet of
1019 the same mice described above from (*RORc(t)*^{Cre} *Vipr2*$^{+/+}$ or *RORc(t)*^{Cre} *Vipr2*$^{fl/fl}$ mice).
1020 **e,** Phylogenetic profile of the microbiota composition in the fecal pellet of *RORc(t)*^{Cre}
1021 *Vipr2*$^{+/+}$ or *RORc(t)*^{Cre} *Vipr2*$^{fl/fl}$ mice after 12h of feeding.
1022
1023 **Extended Data Figure 11. Feeding increase the efficiency of triglyceride**
1024 **absorption. a, b,** Plasma ^{3}H CPM (counts per minute) in mice fed or fasted for 12h
1025 during the light-phase (ZT 0 – ZT 12, red and green circles) or during the dark-phase
1026 (ZT 12 – ZT 0, blue and black circles) and then gavaged with ^{3}H-triolein and sampled at
1027 different times (**a**); and AUC during 4h **(b)**. AUC: Area under the curve per mL of
1028 plasma. N=4 mice per group, representative of two independent experiments, *$P < 0.05$
1029 and ****$P < 0.001$ (two-way ANOVA). **c,** Weight of 10 littermate/cagemate pairs of
1030 *RORc(t)*^{Cre} *Vipr2*$^{+/+}$ and *RORc(t)*^{Cre} *Vipr2*$^{fl/fl}$ mice under regular chow diet (male, 9 weeks
1031 old). Representative of two independent experiments, **$P < 0.01$ (*t-test*). **d,** Weight
1032 difference (%) between each *RORc(t)*^{Cre} *Vipr2*$^{fl/fl}$ mouse compared to its paired

1033 *RORc(t)*^{Cre} *Vipr2*$^{+/+}$ littermate/cagemate. **e,f,** Graphical abstract **(e)** and theoretical

1034 model **(f)** of the observations described created with BioRender.

1035

1036 **Supplementary Videos**

1037 **Supplementary Video 1.** 3D software reconstruction of Figure 1b showing the small intestine

1038 of *Rorc(t)*$^{EGFP/+}$ mice with a cluster of intestinal ILC3 (cryptopatch) in close proximity to enteric

1039 neurons. Pan-neuronal marker: β3-tubulin^{+} (red), ILC3: GFP^{+} (green, respectively).

1040

1041 **Supplementary Video 2.** 3D software reconstruction of Figure 1c from the small intestine of

1042 *Rorc(t)*$^{EGFP/+}$ mice showing ILC3 in the cryptopatch in close proximity to enteric neurons in the

1043 small intestine lamina propria. Pan-neuronal marker: β3-tubulin^{+} (red), ILC3: GFP^{+}TCRβ^{neg}

1044 (green, respectively).

1045

1046 **Supplementary References**

1047 36. Eberl G, Littman DR. Thymic origin of intestinal alphabeta T cells revealed by fate
1048 mapping of RORgammat+ cells. *Science.* 2004;305(5681):248-251.
1049 37. Lochner M, Peduto L, Cherrier M, et al. In vivo equilibrium of proinflammatory IL-17+
1050 and regulatory IL-10+ Foxp3+ RORgamma t+ T cells. *J Exp Med.* 2008;205(6):1381-1393.
1051 38. Wang H, Yang H, Shivalila CS, et al. One-step generation of mice carrying mutations in
1052 multiple genes by CRISPR/Cas-mediated genome engineering. *Cell.* 2013;153(4):910-
1053 918.
1054 39. Yang H, Wang H, Jaenisch R. Generating genetically modified mice using CRISPR/Cas-
1055 mediated genome engineering. *Nat Protoc.* 2014;9(8):1956-1968.
1056 40. Zhang F, Zarkada G, Han J, et al. Lacteal junction zippering protects against diet-induced
1057 obesity. *Science.* 2018;361(6402):599-603.
1058 41. Bankhead P, Loughrey MB, Fernandez JA, et al. QuPath: Open source software for digital
1059 pathology image analysis. *Sci Rep.* 2017;7(1):16878.
1060 42. Caporaso JG, Lauber CL, Walters WA, et al. Ultra-high-throughput microbial community
1061 analysis on the Illumina HiSeq and MiSeq platforms. *ISME J.* 2012;6(8):1621-1624.
1062 43. Bolyen E, Rideout JR, Dillon MR, et al. Reproducible, interactive, scalable and extensible
1063 microbiome data science using QIIME 2. *Nat Biotechnol.* 2019;37(8):852-857.

1064 44. Lugering A, Ross M, Sieker M, et al. CCR6 identifies lymphoid tissue inducer cells within
1065 cryptopatches. *Clin Exp Immunol.* 2010;160(3):440-449.
1066 45. Reynders A, Yessaad N, Vu Manh TP, et al. Identity, regulation and in vivo function of gut
1067 NKp46+RORgammat+ and NKp46+RORgammat- lymphoid cells. *EMBO J.*
1068 2011;30(14):2934-2947.

1069

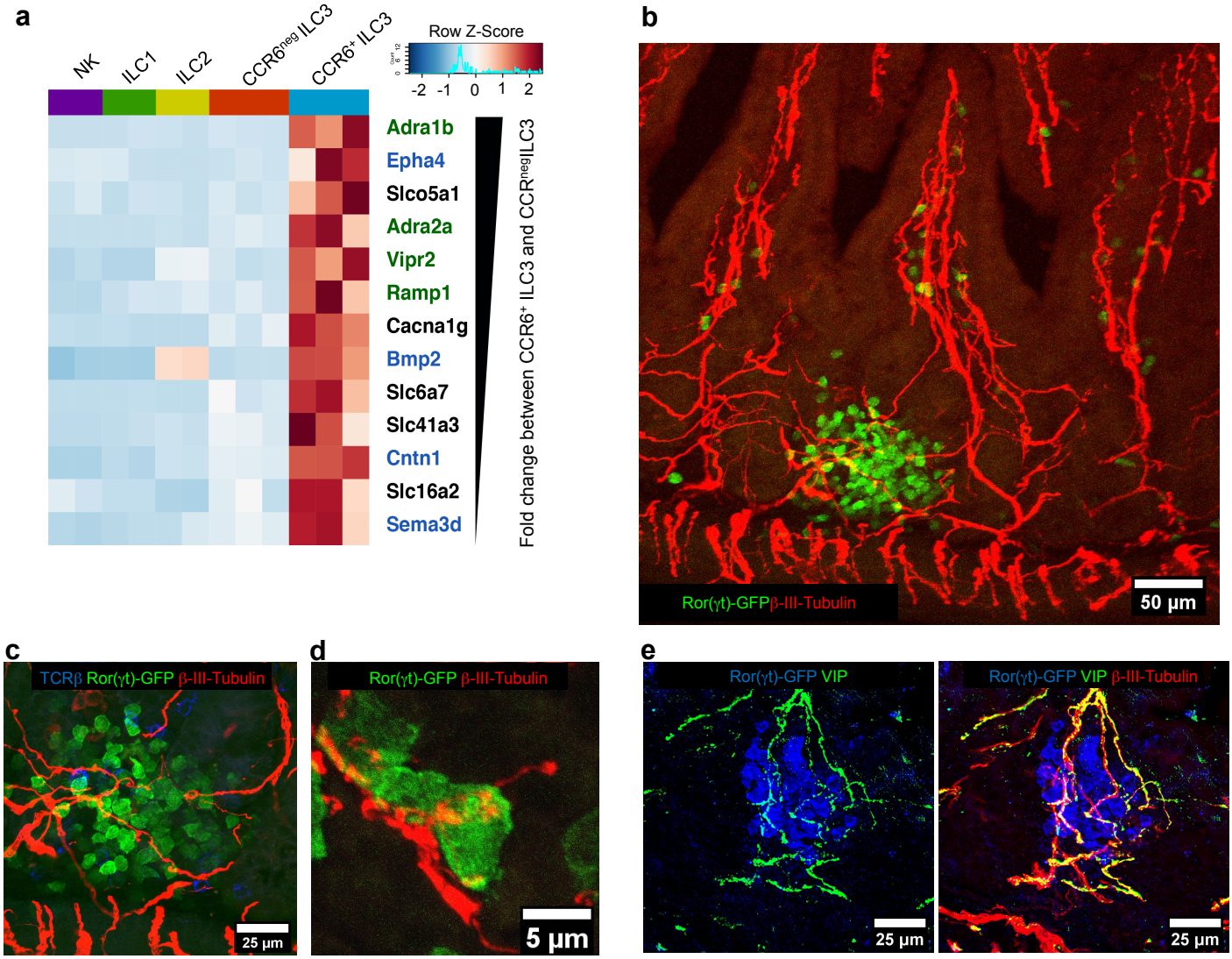

Figure 1. Processes of VIP-producing enteric neurons are in close proximity to *Vipr2*-expressing ILC3 within cryptopatches. a, Heatmap of differentially expressed neural-related genes between intestinal CCR6^{+} ILC3 and CCR6^{neg} ILC3 (Fold change $\geq$ 2, *p-value <0.05,* GSE116092). Color scale is based on normalized read counts. Genes are listed on the right hand margin ranked based on the relative fold change, and color coded: Green: Neurotransmitter/neuropeptide receptors, Blue: genes related to nervous system development/axonal guidance and contact. Expression in other ILC subsets is included for comparison. **b-d,** Representative confocal images from the small intestine of *RORc(t)*$^{EGFP/+}$ mice show clusters of intestinal ILC3 (cryptopatch) in close proximity to enteric neurons in the small intestine lamina propria (see supplementary videos 1 and 2). Pan-neuronal marker: β3-tubulin^{+} (red), ILC3: GFP^{+}TCRβ^{neg} (green and blue, respectively). n=4 mice, all the 110 ILC3 clusters analyzed exhibited β3-tubulin^{+} fibers interacting with ILC3. **e,** Neurochemical code of cryptopatch-associated enteric neurons. Representative confocal images from the small intestine of *RORc(t)*$^{EGFP/+}$ mice show cryptopatch-associated enteric neurons are positive for VIP. Neurons: β3-tubulin^{+} (red), VIP^{+} (green); ILC3: GFP^{+} (blue). n=4 mice, 40 ILC3 clusters analyzed, with all displaying VIP^{+} β3-tubulin^{+} fibers interacting with ILC3.

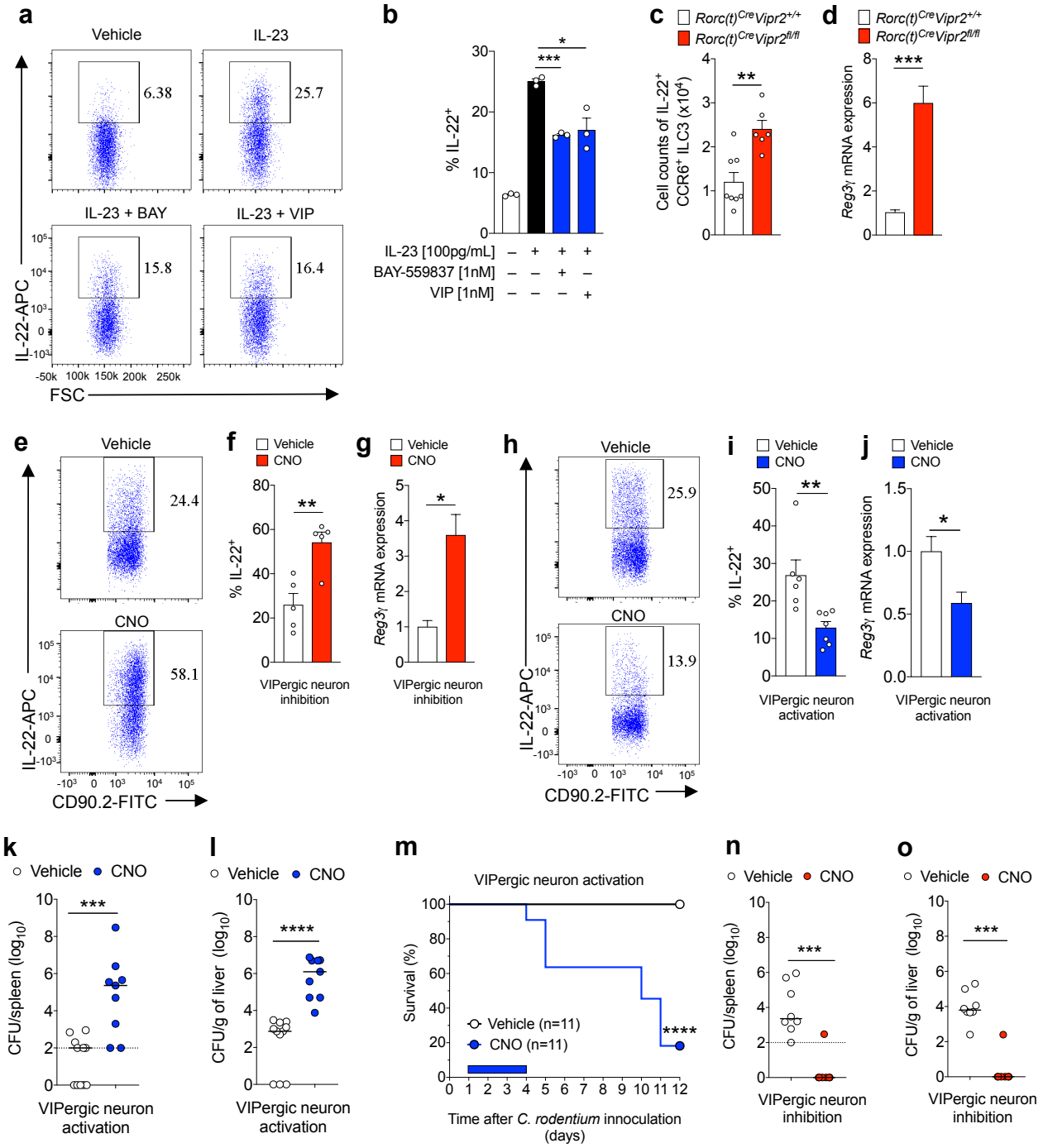

Figure 2. VIPergic signaling promotes reduction of mucosal barrier function by VIPR2-dependent inhibition of CCR6⁺ ILC3. a, b, Representative FACS plot (**a**) and summaries (**b**) indicating IL-22 expression in purified CCR6⁺ ILC3 after *in vitro* IL-23 stimulation with/without VIPR2 agonist ligands. BAY: BAY-559837, VIP: vasoactive intestinal peptide. **P*<0.05 and ****P*<0.001 (*t-test*). Data are representative of three independent experiments. **c,** Number of IL-22⁺ CCR6⁺ ILC3 present in the ileum of *RORc(t)*^{Cre}*Vipr2*$^{+/+}$ and *RORc(t)*^{Cre} *Vipr2*$^{fl/f}$ mice. *RORc(t)*^{Cre}*Vipr2*$^{+/+}$: 8; *RORc(t)*^{Cre} *Vipr2*$^{fl/f}$: 6. Data are representative of 2 independent experiments, ***P*<0.01 (*t-test*). **d,** Normalized *RegIIIγ* mRNA expression in IEC-enriched ileal extracts from *RORc(t)*^{Cre}*Vipr2*$^{+/+}$ and *RORc(t)*^{Cre} *Vipr2*$^{fl/f}$ mice. *RORc(t)*^{Cre}*Vipr2*$^{+/+}$: 5; *RORc(t)*^{Cre} *Vipr2*$^{fl/f}$: 5. Data are representative of 3 independent experiments,****P*<0.001 (*t-test*). **e-g,** Effect of VIPergic inhibition on ILC3 and IECs. Representative FACS plot (**e**) and summary (**f**) indicating IL-22 expression in CCR6⁺ ILC3 from the ileum of *Vip*$^{IRES\text{-}Cre}$*hM4Di*$^{fl\text{-}stop\text{-}fl/+}$ mice (DREADD for VIPergic inhibition) at 24h following treatment with vehicle or CNO (Clozapine-N-oxide, DREADD ligand). Vehicle: n=5, CNO: n=5. ***P*<0.01 (*t-test*). Data representative of three independent experiments. **g,** Normalized *RegIIIγ* mRNA expression in ileal extracts enriched for IECs at 24h following treatment. Vehicle: n=3, CNO: n=3. **P*<0.05 (*t-test*). Data representative of two independent experiments.

Continuation Figure 2. h-j, Effect of VIPergic activation on ILC3 and ileal extracts enriched for IECs. Representative FACS plot (**h**) and summaries (**i**) indicating IL-22 expression in CCR6^{+} ILC3 from ileum of *Vip*$^{IRES\text{-}Cre}$*hM3Dq*$^{fl\text{-}stop\text{-}fl/+}$ (DREADD for VIPergic activation) at 24h following the treatment with vehicle or CNO. Vehicle: 6, CNO: 7. ***P*<0.01 (*t-test*). **j,** Normalized *RegIIIγ* mRNA expression in ileal extracts enriched for IECs at 24h following treatment with vehicle or CNO. Vehicle: 7, CNO: 6. **P*<0.05 (*t-test*). Data representative of three independent experiments. **k, l,** Dissemination of *C. rodentium* to the (**k**) spleen and (**l**) liver in *Vip*$^{IRES\text{-}Cre}$*hM3Dq*$^{fl\text{-}stop\text{-}fl/+}$ mice treated with vehicle or CNO (1mg/Kg, daily) for 4 days post-intragastric infection with 2x10^{9} CFU. Log_{10} Colony Forming Units (CFU) of *C. rodentium* 9 days post-oral innoculation (9 d.p.i.). Dotted line: limit of detection. ****P*=0.0009 and ****P<0.0001, (*Mann-Whitney test*). Vehicle: n=11 (Positive for *C. rodentium:* spleen: 6/11, liver: 8/11), CNO: n=9 (Positive for *C. rodentium:* spleen and liver: 9/9). Data representative of two independent experiments. **m,** Survival rates for *C. rodentium*-infected *Vip*$^{IRES\text{-}Cre}$*hM3Dq*$^{fl\text{-}stop\text{-}fl/+}$ mice treated with vehicle or CNO (1mg/Kg, daily, 1-4 d.p.i.: blue rectangle). Vehicle: n=11, CNO: n=11. Data representative of three independent experiments. *****P*<0.0001 *(Mantel-Cox test*). **n, o,** Bacterial dissemination to the (**n**) spleen and (**o**) liver of *Vip*$^{IRES\text{-}Cre}$*hM4Di*$^{fl\text{-}stop\text{-}fl/+}$ mice treated with vehicle or CNO (1mg/Kg, daily, 1-4 days post-intragastric infection with 4x10^{10} CFU of *C. rodentium*). Log_{10} CFU at 9 d.p.i. Dotted line: limit of detection. Vehicle: n=8 (Positive for *C. rodentium:* spleen: 8/8, liver: 8/8), CNO: n=7 (Positive for *C. rodentium:* spleen: 1/7, liver: 1/7). ****P*=0.0006 (spleen) and ****P*=0.0005 (liver) (*Mann-Whitney test*)**.** Data representative of two independent experiments. **k,l,n,o**: For visualization in the logarithm scale, CFU counts of 0 were attributed a value of 1.

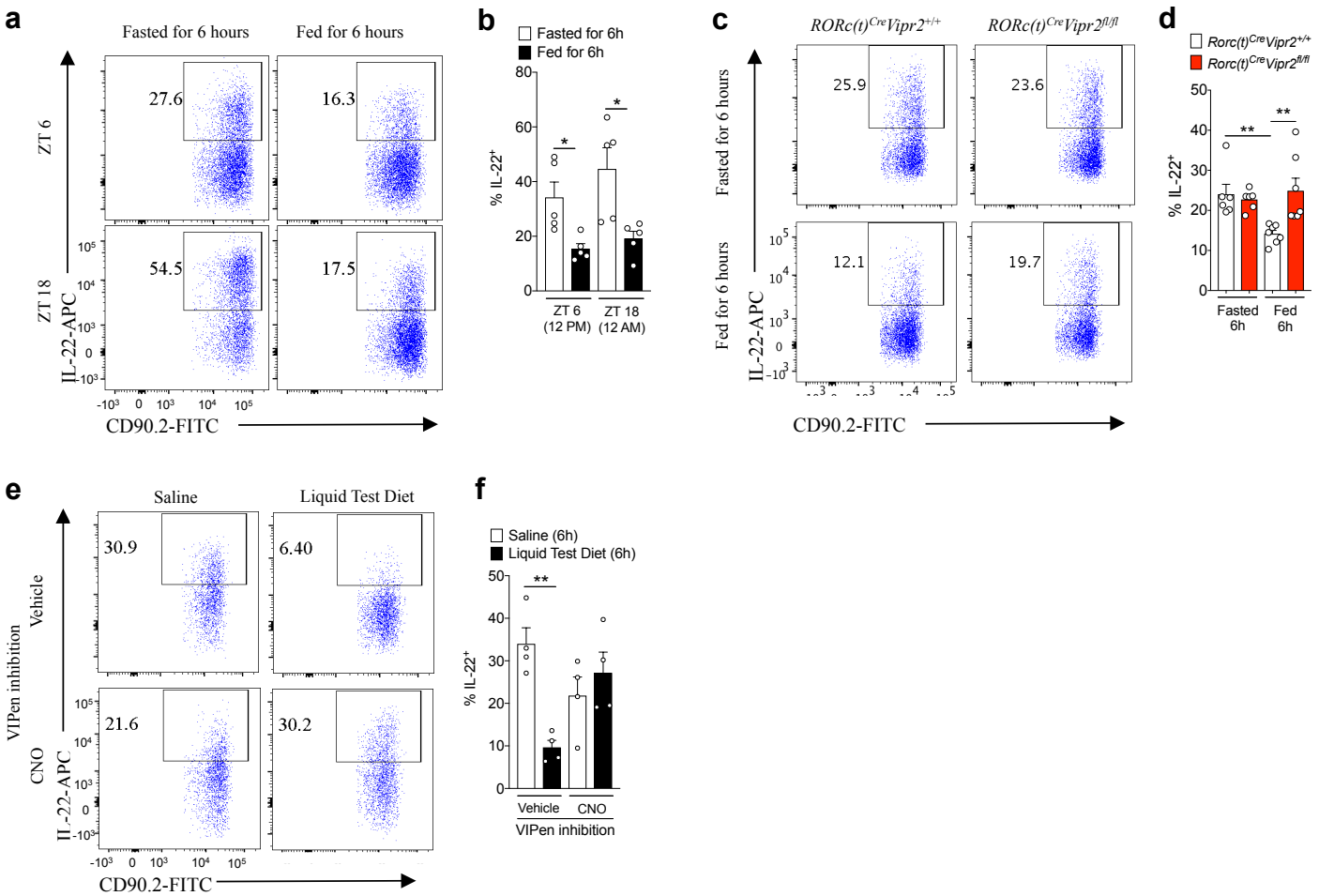

Figure 3. Feeding reduces IL-22 production by CCR6⁺ILC3 through activation of VIPergic neurons. a, b, Representative FACS plot (**a**) and summaries (**b**) indicating IL-22 expression among CCR6⁺ ILC3 from the ileum of mice at 6h after feeding or fasting, at ZT6 and ZT18. N=5, *P<0.05 (*t-test*). Data are representative of two independent experiments. **c, d,** Representative FACS plot (**c**) and summaries (**d**) indicating IL-22 expression by CCR6⁺ ILC3 from *RORc(t)*^{Cre}*Vipr2*$^{+/+}$ or *RORc(t)*^{Cre}*Vipr2*$^{fl/fl}$ mice at 6h after fasting or 6h after feeding (ZT 18). **P<0.01 (*paired t-test*). Data shown are pooled from two independent experiments and representative of three independent experiments. **e, f,** Representative FACS plot (**e**) and summaries (**f**) indicating IL-22 expression in CCR6⁺ ILC3 from the ileum of *Vip*$^{IRES\text{-}Cre}$*hM4Di*$^{fl\text{-}stop\text{-}fl/+}$ mice (DREADD for VIPergic inhibition). Mice were treated with vehicle or CNO (1mg/Kg) and 30 minutes later were fed by intragastric administration of saline (0.4 mL each 45 min, for 6 h) or Liquid Test Diet (500 mg/mL, 0.4mL each 45 minutes, for 6 h). N=4, **P<0.01 (*t-test*). Data shown are representative of three independent experiments.

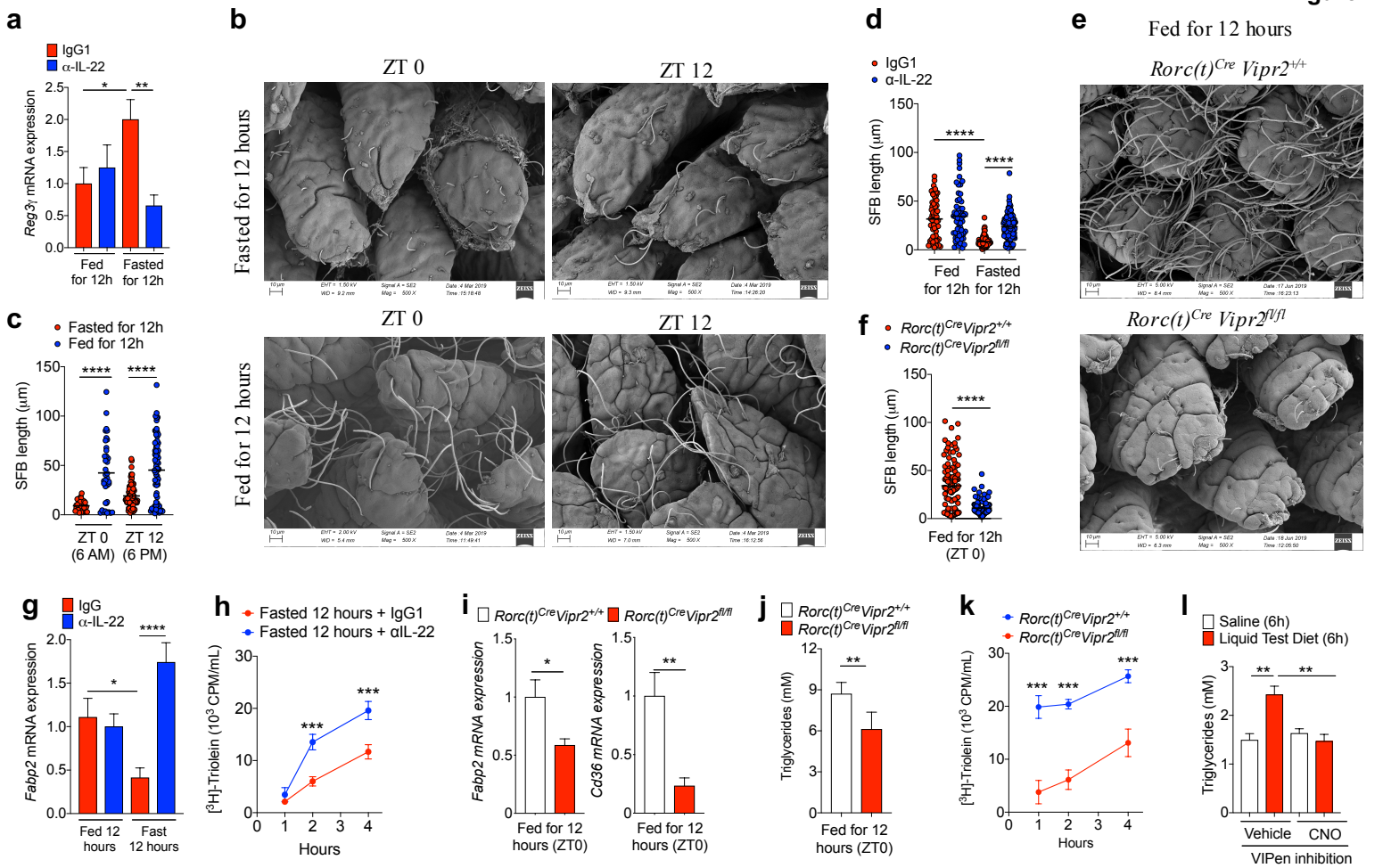

Figure 4. Dynamic regulation of commensal bacterial growth and lipid absorption by feeding-dependent modulation of the VIP-VIPR2-IL-22 axis. a, Normalized *RegIIIγ* mRNA expression in IECs from mice treated with IgG or α-IL-22 (10mg/Kg) during the feeding period (Fed for 12h: Treated from ZT 12->ZT 0) or during the fasting period (Fasted for 12h: Treated from ZT 0->ZT 12). Data pooled from 2 independent experiments: Fed IgG1: N=8, Fed α-IL-22: N=8, Fasted IgG1: N=8, Fasted α-IL-22: N=7, *P<0.05 and **P<0.01 (*t-test*). **b, c,** Representative scanning electron microscopy (SEM) images (**b**) of epithelium-associated commensal SFB in the ileum of mice 12h after fasting or feeding at the end of the dark-phase (ZT 0) and the light-phase (ZT 12) and (**c**) measurements of SFB filament lengths. N=3, data representative of 2 independent experiments,****P<0.001 (*t-test*). **d,** SFB length in the ileum of mice treated with IgG or α-IL-22 (10mg/Kg) during the feeding period (Fed for 12h: ZT 12->ZT 0) or during the fasting period (Fast for 12h: ZT 0->ZT 12). N= 3, data representative of 2 independent experiments,****P<0.001 (*t-test*). **e,f,** Representative **(e)** SEM images of epithelium-associated SFB in the ileum of *RORc(t)^{Cre} Vipr2$^{+/+}$* and *RORc(t)^{Cre} Vipr2$^{fl/fl}$* mice fed for 12h and **(f)** measurement of bacterial filament lengths. N= 3, ****P<0.001 (*t-test*). **g,** Normalized *Fabp2* mRNA expression in IEC-enriched ileal extracts from mice treated with IgG or α-IL-22 (10mg/Kg) during the fasting period (Fasted for 12h: Treated from ZT 0->ZT 12). Data representative of 3 independent experiments: Fed IgG1: N=8, Fed α-IL-22: N=8, Fast IgG1: N=8, Fed α-IL-22: N=7. *P<0.05 and ****P<0.0001 (t-student). **h,** Plasma ^{3}H CPM (counts per minute) in 12h fasted mice after gavage with ^{3}H-triolein (2uCi/mice in 200ul of 20% Intralipid). Mice were treated with IgG or α-IL-22 (10mg/Kg) during the fasting period (Fasted for 12h: Treated from ZT 0->ZT 12). Data representative of 2 independent experiments. N=4, ***P<0.001 (*two-way ANOVA*). **i, j,** Normalized *Fabp2* and *Cd36* mRNA expression in IEC-enriched ileal extracts from (**i**) and plasma triglyceride content (**j**) in 12h fed *RORc(t)^{Cre} Vipr2$^{+/+}$* (N=5) and *RORc(t)^{Cre} Vipr2$^{fl/fl}$* (N=4) mice. *P<0.05 and **P<0.01 (*t-test*). **k,** Plasma ^{3}H CPM in 12h fed *RORc(t)^{Cre} Vipr2$^{+/+}$* (N=3) and *RORc(t)^{Cre} Vipr2$^{fl/fl}$* (N=3) mice after gavage with ^{3}H-triolein. Data representative of 2 independent experiments,***P<0.001, (*two-way ANOVA*). **l,** Plasma triglyceride content in *Vip$^{IRES\text{-}Cre}$hM4Di$^{fl\text{-}stop\text{-}fl/+}$* mice (DREADD for VIPergic inhibition) after gavage with Saline (0.4 mL/each 45 minutes, for 6 hours) or Liquid Test Diet (500 mg/mL, 0.4mL/each 45 minutes, for 6 hours). Vehicle: N=5, CNO: N=4. Data representative of 2 independent experiments, **P<0.01, (*t-test*).